A Novel Processing Route for the Fabrication of Porous Magnesium Biomaterials

A thesis

submitted in partial fulfilment

of the requirements for the Degree

of

Master of Engineering

in the

Department of Mechanical Engineering

University of Canterbury

by

Jerawala Huadmai

University of Canterbury

Christchurch, New Zealand

2005

ABSTRACT

Metallic biomaterials continue to play an essential role to assist with the repair or replacement of natural bone that has become diseased or damaged. Metals have high mechanical strength making them better suited to load-bearing applications than polymeric and ceramic biomaterials [1]. At present, stainless steel, Co-Cr alloys and Ti alloys are three main metallic biomaterials used as bone prosthesis [2, 3]. Although these metals are, in monolithic form, biocompatible, fine debris particles and/or ions released over the lifetime of the implantation, coming into contact with the surrounding tissue appear to be not biocompatible. The abnormally high levels of metal ions and/or particles are believed to be associated with carcinogenic, toxic, inflammatory and allergic reactions eventually leading to the prosthesis aseptic loosening [4-10]. High mechanical stiffness of the three metals is also believed to associate with bone resorption – a situation where bone around the implant becomes thinner or more porous. The high stiffness metal, once implanted, changes the distribution of applied load in the adjacent bone [11, 12].

Recently, there have been interests in using magnesium and its alloy as a metallic biomaterial. Magnesium is a bioresorbable metal with an ability to enhance bone healing process [13, 14]. It also has lower stiffness making it more resemble to that of natural bone in terms of mechanical properties.

This work presented in this thesis involves an investigation a manufacturing route that is feasible and viable for producing Mg foam for tissue engineering and bone implant

applications. The microstructure and mechanical properties of Mg foam is studied and tested then compared with natural human bone.

ACKNOWLEDGEMENTS

"Do not go where the path may lead, go instead where there is no path and leave a trail"

I am so relieved and happy that this challenging project finally came to an end. Because I love the challenge I jumped to this project despite I know that I had limited background knowledge required to master it. And because of this fact, I deeply know that my supervisor, Dr. Mark Staiger, had to put a huge effort into this project. I have no word else to say but thank you for being so encouraging and supportive supervisor. I very much owe this success to him.

I would like to specially thank to Mike Flaws who without him Mg would never been cast. Thanks for spending a lot of time casting Mg and giving good ideas to solve experimental problem to me. One person I must not forget is Michale Raynolds – thanks for the idea and starting point you made that was vital to the success of this project. Thanks also to Kevin Stobbs for helping me setting up lab equipments and general lab works. I would like to thank you both – Julian Phillips and Julian Murphy – for your kindness and your dedicated work. I must thank to workshop guys -- Scott Amies, Pual Wells and Ken Brown -- for letting me interrupt their work with my always-urgent work. I do appreciate your patience with me. Big thank to Sato, Azmi, Sandra, Ben, Haiyuan, Hamish, Matt and everyone in Materials Engineering Group. Special thanks to my colleagues in Thailand. Especially you – Nattaka Yokakul, thanks for always being there when I need help. Last but most importantly, I have to thank to my beloved family, especially my sister, Charuwalee Huadmai. You never know how much your success inspires me and keeps me improving myself.

TABLE OF CONTENTS

LIST OF FIGURES

LIST OF TABLES

Nomenclature

Biodegradable	Solid materials and devices which break down due to macromolecular degradation with dispersion in vivo leaving some fragments that do not necessarily leave the body entirely and may, in some applications, elicit harmless host responses (summarised from [15, 16]).
Bioresorbable	Solid materials and devices which show bulk degradation and further resorb in vivo with no residual side effects. They may be metabolised into proteins or eliminated from the body. (summarised from [15, 16]).
BMP (Bone marrow protein)	A cytokine known for its unique characteristic of inducing bone when it was implanted with a certain carrier into ectopic tissues such as skin or tissue.
Cytotoxic	Cytotoxic substance is toxic to cells
Epidemiology	1: a branch of medical science that deals with the incidence, distribution, and control of disease in a population 2 : the sum of the factors controlling the presence or absence of a disease or pathogen
Integrins	One of a large and very important family of adhesion molecules that promote stable interactions between cells and their environment. The integrins also act as cellular sensor and signaling molecules. Integrins contain two types of subunits called alpha and beta. All of the alpha subunits have some similarity to each other, as do all of the beta subunits [17].
Osteoblasts	Bone cells that initiate bone formation process by excreting the substance called collagen molecules which afterwards becomes denser and forms a collagen matrix, which provides a platform for mineral to be deposited on during the mineralisation process [18]
Osteocytes	One of bone cells derived from osteoblasts and embedded in the body of bone [18].
Osteoclasts	Bone cells responsible for absorption of bone; derived from monocyte or monocyte-like cells, which are the cells circulating in the blood. Osteoclasts attach themselves on the bone surface and absorb the bone by secreting some substances (enzymes and acids) that dissolve bone. Osteoclasts are large, multinucleated cells (on average contains 2–10 nuclei but may consists up to 50 nuclei) [18-20]. Size of osteoclasts depends on number of nuclei they have, for example, around 160 μm for large osteoclastic cell with more than 10 nuclei [21].
Tissue engineering	An interdisciplinary field that applies the principles of engineering and life sciences toward the development of biological substitutes that restore, maintain, or improve tissue function.

1. Introduction

1.1 Human bone

1.1.1 Structure of bone

Bone is a highly dense matrix tissue, which, at the nano-scale, is composed principally of collagen fibre mineralised with crystal of calcium phosphate and small amount of a *ground substance*. Ground substance is a homogeneous gelatinous medium consisting mainly of extracellular fluid plus proteoglycans that are protein-substituted carbohydrates. Calcium-phosphate is also known as "hydroxyapatite" (HA). The chemical composition of pure HA can be given as $Ca_{10}(PO_4)_6(OH)_2$. Human natural bone, however, is not pure HA but also contains trace elements as listed in Table 1.1. Usually the bone of adults consists of approximately 50% by volume HA [18, 19, 22]. Collagen fibre functions as the matrix in bone. It gives bone its toughness while hydroxyapatite stiffens the bone structure [18, 19].

Macroscopically, there are two types of bone: compact (or cortical bone) and cancellous (or spongy bone). Cancellous bone is more porous than cortical bone. Bone with a porosity higher than 30% can be regarded as cancellous bone [23]. Cortical bone is mostly located in the shaft or long bone while cancellous bone is largely present in flat bone and at an end of long bones. The structure of long bone consists of cortical bone surrounding the cancellous bone and marrow cavity (see Figure 1.1). Thus, a sandwich-like structure is formed containing dense hard material as the outer skin with porous material at the core [22, 24, 25].

Table 1.1 Chemical composition of human bone apatite.

Composition	**Weight %**	
	Daculsi [26]	Dorozhkin [27]
Calcium (Ca^{2+})	24.5	34.8
Phosphorus (P)	11.5	15.2
Carbonate (CO_3^{2-})	5.8	7.4
Sodium (Na^+)	0.7	0.9
Magnesium (Mg^{2+})	0.55	0.72
Chloride (Cl^-)	0.1	0.13
Pyrophosphate (P_2O7)	0.07	0.07
Potassium (K^+)	0.03	0.03
Fluoride (F^-)	0.02	0.03
Ash (total inorganic)	65	65
Total organic	25	25
Adsorbed H_2O	9.7	10
Trace elements: Sr^{2+}, Pb^{2+}, Fe^{3+}, Zn^{2+}, Cu^{2+}, etc.		

Figure 1.1 shows the cross section of some skeletal bones. At low density, cancellous bone is an open-cell structure constructed from interconnected network of cylindrical struts, about 0.1 mm in diameter and 1 mm in length. The network of struts of low-density cancellous bone are arranged with no preferred orientation and this kind of structure is generally found where the applied load or stress is low such as vertebrae. At higher density, the structure of bone becomes more like a plate-like with a size that extends up to several millimetres. The plate-like structure has a preferential orientation of the trabeculae and occasionally appears to be almost closed cell. Plate-like cancellous bone is likely to be found where a constant stress is applied [18, 23]. The type of structure and porosity of bone due to the level of applied stress is thought to rely on the ability of bone to generate an electric potential. This electric potential is believed to be a factor controlling bone growth [23].

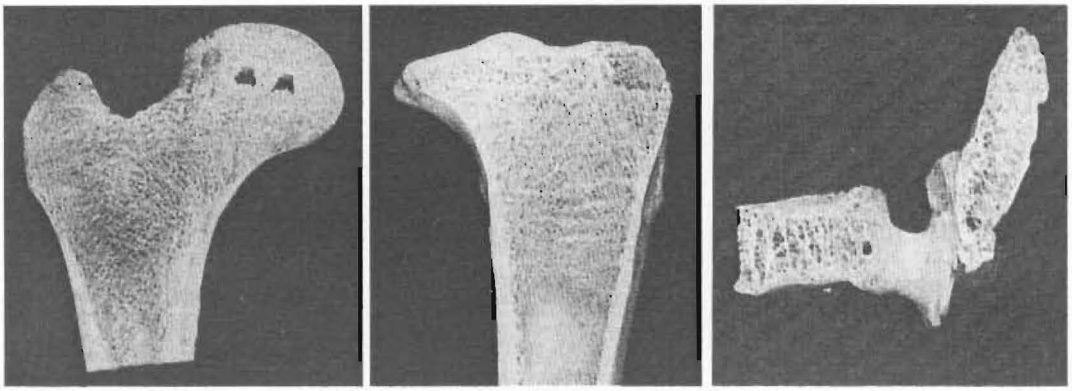

(a) (b) (c)

Figure 1.1 Longitudinal cross-section of (a) the end of a human femur, (b) tibia and (c) lumbar vertebra [23].

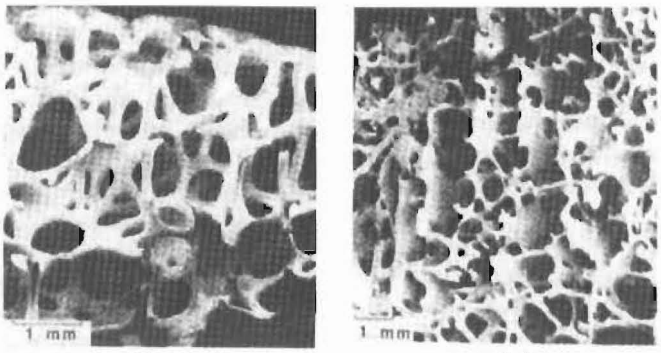

(a) (b)

Figure 1.2 Structures of cancellous bone at various densities. (a) An open-cell structure with low density. (b) A parallel-plate-like structure with higher density, showing the preferential orientation [23].

1.1.2 Mechanical Properties of bone

The density (or porosity) of cancellous bone varies due to the differences in magnitude of loads applied on it. Higher applied stresses cause the formation of denser bone. The differences in density result in the differences in mechanical properties and behaviour of both compact and cancellous bones. The density of cortical bone also varies although very small compared to that of cancellous bone. Therefore, mechanical properties of cortical bone are relatively predictable. Table 1.2 summarises the mechanical properties of cortical bone based on the literature.

Table 1.2 The properties of cortical bone.

Sources	Gibson [23]	Summarised from Currey [18]
Density, ρ (g/cm^3)	1.8-2.0	
Young's modulus, E_s (GPa)		
longitudinal	17.0	20.0
radial	11.5	12.0
Shear modulus, G_s (GPa)	3.3	5.6
Compressive strength, σ_{ys} (MPa)		
along	193	205-213
normal	133	131
Tensile yield strength, σ_{ys}^{T} (MPa)		
along	148	128-133
normal	49	53

Characterising the mechanical properties of cancellous bone is complex. Generally, the mechanical properties of cancellous bone have been either based on the bone *material* or bone *tissue* [18] – some authors have also used the *trabeculae* and *trabecular* instead [23]. Bone *material* is the solid substance forming an individual trabeculae in the cancellous bone structure [18, 23]. Whereas bone *tissue* involves the complete structure of bone and takes its architecture and density into account [18]. Young's modulus of bone material has been reported in several studies and it varies from ~1 to 20 GPa depending on test procedure used [18, 23]. Table 1.3 provides a summary of elastic modulus values of cancellous bone material. Gibson & Ashby have suggested that the values of Young's modulus, compressive strength and tensile strength of the cancellous bone material to be 12 GPa, 136 MPa and 105 MPa, respectively [23].

Table 1.3 Young's modulus of cancellous bone material [18, 23].

Reference	Type of bone	Specific Method	E_s (GPa)
Mechanical tests			
Ryan and Williams (1989)	BF	tension un-machined	0.76 (0.39 dry)
Rho *et al.* (1993)	H T	tension	10.4 (dry)
Kuhn *et al.* (1987)	HT	3-point bending	3.17 (1.5)
Kuhn *et al.* (1989)	H I	3-point bending	3.7 (wet)
Choi *et al.* (1990)	H PT	3-point bending	4.59 (1.60 wet)
Townsend *et al.* (1975)	H PT	buckling unmachined	11.4 (wet)
			14.1 (dry)
Runkle & Pugh (1975)	H DF	buckling	8.69 (3.17 dry)
Ultrasound test			
Ashman & Rho (1988)	B F	ultrasound on trabecular	10.9 (1.6 wet)
	H F		12.7 (1.5 wet)
Rho *et al.* (1993)	H T		14.8 (wet)
	H T		20.7 (wet)
Turner *et al.* (1999)	H F		17.5 (wet)
Nanoindentation			
Turner *et al.* (1999)	H F		18.1 (dry)
Finite element analysis			
Pugh *et al.* (1973)	H DF	2D FEM	$E_s < E_{compact}$
Williams & Lewis (1982)	H PT	2D FEM	1.30
Mente & Lewis (1987)	H F	2D FEM	5.3 (2.6 dry)
Rietbergen *et al.* (1995)	H PT	3D FEM	2.23-10.1
All specimens are of individual trabeculae unless stated otherwise. B = bovine; H = human; F = femur; T = tibia; P = proximal; D = distal; I = ilium			

The study of mechanical properties of bone tissue often focuses on compressive strength and elastic modulus., Cancellous bone has similar compressive behaviour to other cellular materials, i.e. regions of (i) linear elasticity, (ii) plastic deformation and collapse of cell walls and (iii) densification are observed. The end of linear elasticity and beginning of plastic deformation is when damage in trabeculae bone is initiated in low-density bone due to buckling. During the plastic deformation and cell collapse stage, the walls or struts of cancellous bone buckle progressively until the pores in the structure are completely closed. Finally, the densification stage begins where a steep rise in the stress can be observed as the cell wall materials are pressed together.

As shown in Figure 1.3, the mechanical properties of cancellous bone tissue are strongly depend on its apparent density [18, 23]. Figure 1.4 shows compressive strength and elastic modulus of cancellous bone as a function of the relative density of cancellous bone tissue and the arrangement of trabeculae with respect to the loading direction [23]. Cancellous bone with its prismatic cell structure exhibits values of compressive strength varying from ~0.2 to 9 MPa and an elastic modulus ranging from less than 10 MPa to less than 1 GPa [23].

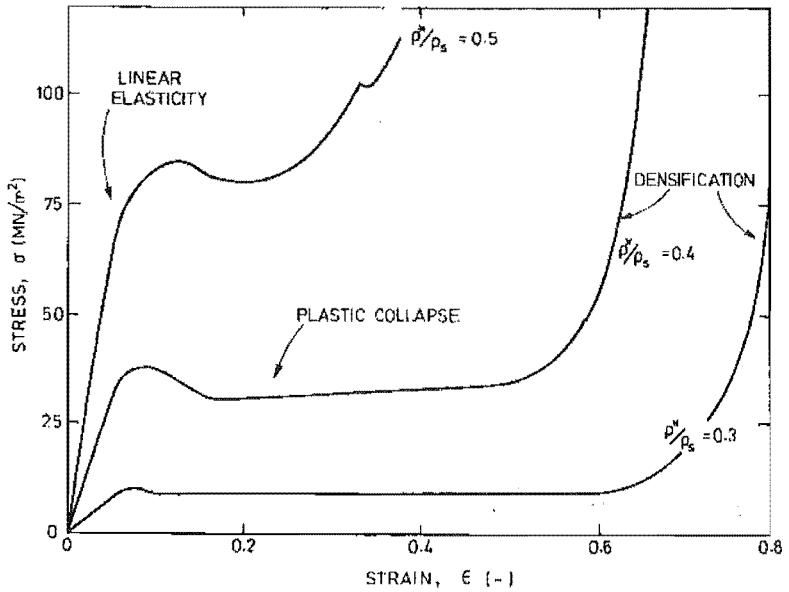

Figure 1.3 Compressive stress-strain curve of cancellous bones at various densities [23].

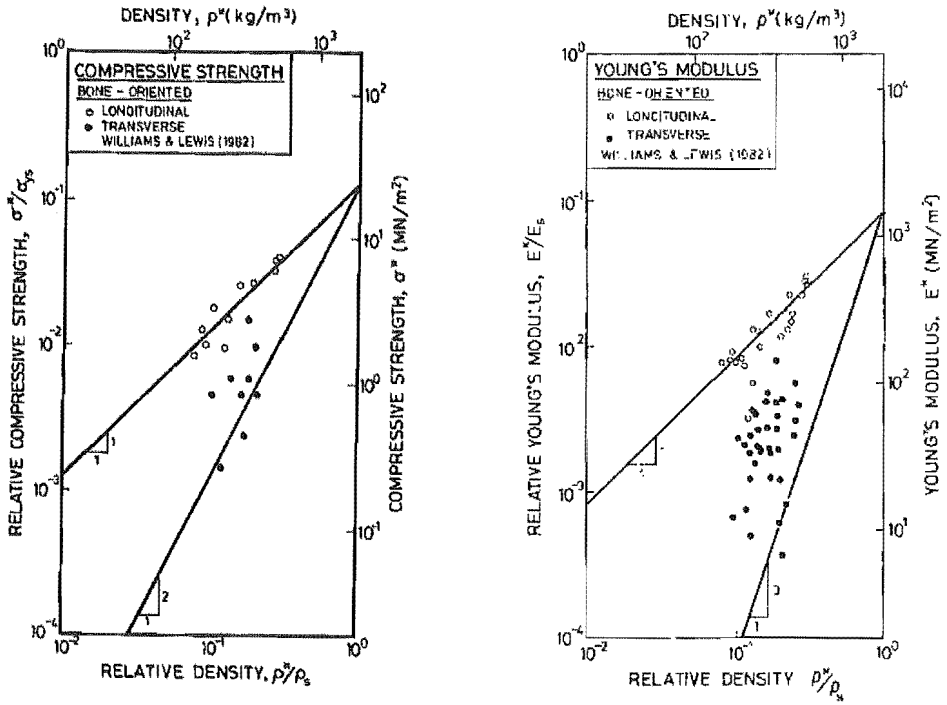

Figure 1.4 Mechanical properties of cancellous bone with prismatic cell structure as a function of relative density a) compressive strength and b) elastic modulus.

1.1.3 Current problems of presently used osteoprostheses

Metallic biomaterials continue to play an essential role to assist with the repair or replacement of natural bone that has become diseased or damaged. Metals have high mechanical strength making them better suited to load-bearing applications than polymeric biomaterials. An exception is UHMWPE which is used in load-bearing applications such as the acetabular cup and tibial plate [28]. However, the use of UHMWPE has disadvantages associated with inflammatory responses to wear debris. Ceramic biomaterials are also used extensively in bone tissue engineering applications. However, the brittle fracture behaviour of bioceramics is still a major drawback where structural support is a requirement [4, 29-31]. Hence, bioceramics are mostly used in low load-bearing applications such as bone plates, bone screws, femoral head and bioactive coatings [29, 30].

Approved metallic biomaterials include stainless steel, cobalt-chromium, and titanium-based alloys. Stainless steel was first introduced to replace vanadium steel which failed to provide adequate corrosion resistance *in vivo* [3]. Co-Cr based alloys have been utilised for their high corrosion resistance compared with Ti, excellent fatigue resistance and high abrasion resistance [2, 3, 32]. Ti alloys have also been highly successful as implant materials due to its excellent biocompatibility, low density and high corrosion resistance [2, 4].

Stainless steel, cobalt-chromium and titanium-based alloys are regarded as biocompatible materials. However, fine debris particles and/or ions released over the lifetime of the implantation, coming into contact with the surrounding tissue appear to be not as biocompatible as in their monolithic form. A long-term clinical study of a patient with a total hip replacement found metal ion concentrations in the blood, serum and urine several times higher than normal [5, 6]. Also, the number of particles produced per year from metal-on-metal contact was calculated to be 6.7×10^{12} to 2.5×10^{14} – ten times higher than that produced by metal-on-polyethylene contact [5]. The abnormally high levels of metal ions and/or particles are believed to be associated with carcinogenic, toxic, inflammatory and allergic reactions [4-9]. The excretion of bone-resorbing cytokines also appears to be enhanced by the presence of particles and/or ions released from stainless steel, cobalt-chromium and titanium-based alloys. Bone-resorbing cytokines are thought to be responsible for loss of bone surrounding an implant, and subsequent aseptic loosening of the implant, due to increased osteoclast differentiation and/or alterations to osteoblastic activities [33-39].

The mismatch between stiffness of bone and that of current metallic biomaterials is also of a concern. High stiffness metal, when implanted, alters load distribution by carrying most of the load. This alteration minimises an amount of load transferred to bone in close proximity to the implant. A reduced load on bone results in bone resorption since bone growth is stimulated by applied stress. This phenomenon is also called stress shielding, a situation where bone becomes more porous and thin. The resorption of bone decreases implant stability and makes revision surgery, if necessary, more difficult [3, 11]. Figure 1.5 demonstrates the mechanical properties of human bone and several current biomaterials. It clearly shows that three main current metallic biomaterials are 1 and 3 orders of magnitude stiffer than human cortical and cancellous bone, respectively.

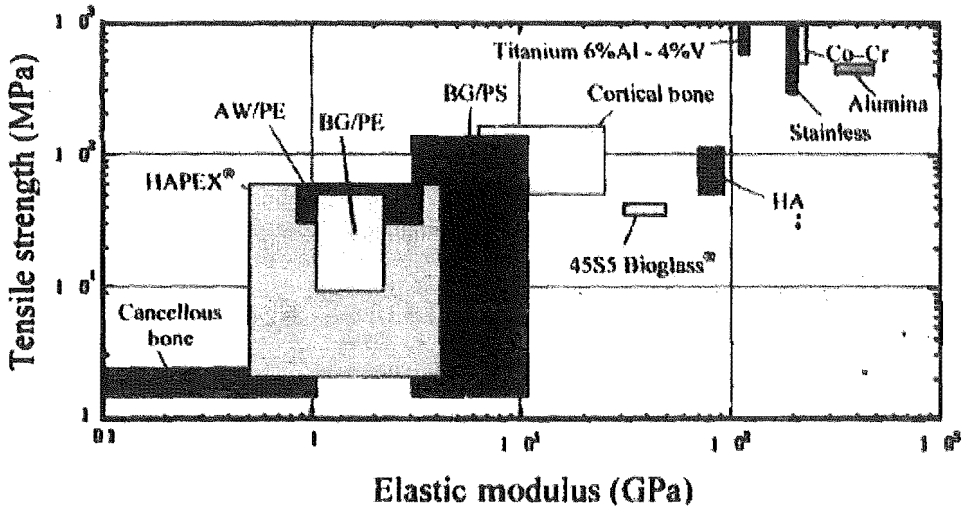

Figure 1.5 Diagram shows the mismatch in mechanical properties between human bone and three conventional metallic biomaterials.

1.1.4 Requirements for bone tissue-engineering biomaterials

As the disadvantages and limitations of transplant technique, such as site infection and morbidity and limited available of suitable donor, the treatment approach has been shifted from tissue replacement to naturally tissue regeneration and restoration [1].

Tissue engineering is the interdisciplinary approach of combining knowledge of life sciences and engineering to develop an organ substitute that possesses useful biological properties to help promote or accelerate restoration of damaged tissue. The approach involves using living cells together with either natural or synthetic materials to produce an implantable scaffolds or devices. For bone implant biomaterials, an ideal tissue engineering biomaterials must satisfy the requirements biologically, structurally and mechanically [15, 40]. Requirements for tissue engineering biomaterials are summarised in the next three sections of this report.

1.1.4.1 Bioresorbability

The implant scaffold provides a template for regenerated tissue. The scaffold shouldn't be permanently present in human body in order to avoid any unforeseen advert affects such as interfacial stability with host tissue, stress shielding (see 1.1.4.3), and mechanical and electrochemical wear debris [1]. Bone precursor cells can be seeded on scaffold pre-operationally and scaffold is then implanted [41, 42] or scaffold is directly implanted in patient's defect site [41]. In either case, scaffold should safely resorb at the rate close to the tissue regeneration rate.

1.1.4.2 Architectural requirements

The desired architectures of orthopaedic materials have been suggested by many researchers. However, there appears to be a common requirement regarding the pore size, porosity and surface topography [43]. A scaffold is designed to act as a template where the regeneration process of new bone tissue takes place. It is crucial that functional cells, such as osteoblast and mesenchymal cells, are able to be transported and allowed to migrate through the scaffold to the area where tissue regeneration is aimed. Thus, it is

desirable that the structure of the scaffold is porous with a network of interconnected pores. The porosity and pore interconnectivity are crucial as they control the level of oxygen and nutrient transportation through the scaffold and, hence, influence the proliferation of functional cells. Pore interconnectivity of scaffold has been increasingly received attention in recent studies compared to characteristic of pore size [15, 41, 42, 44] and newly is regarded as a most important parameter for a scaffold [45]. In order for cells to efficiently move in and out of the scaffold, it is thought that the size of pores should be at least 100 μm [42, 46].

In terms of pore size, implanted scaffolds with too small pore size (<100 μm) result in the formation of an unmineralised osteoid and the creation of fibrous tissue [46, 47]. On the other hand, it has also been suggested that pore size may not need to be larger than 600 μm since this would compromise the mechanical properties as the density decreases [46]. Studies have suggested that the optimum pore size is ~300 μm [42, 46-50]. Investigations of the influence of pore size on formation of bone was carried out in rabbits, with results showing that the level of mineralised bone tissue was found to be highest in 39% porous HA with a pore size range of 175-260 μm as compared to pore size ranges of 260-350 μm and 350-435 μm [47]. In another study it was found that cylindrical pore of ∅300 μm in HA provided the highest bone formation and increment in compressive strength compared to those with cylindrical pore sizes of 50, 100 and 500 μm. It was observed that a pore size of ∅500 μm gave the lowest value when the results were compared in term of strength as a function of macroporosity [50]. The relationship between the density and mechanical properties of a porous structure will be discussed in more detail in section 1.2.3.

Surface morphology is another important characteristic of the scaffold. The existence of micropores on the wall of macropores was shown to be a crucial factor that influences the degree of cell attachment and depth of cell penetration (*i.e.* osteoconductivity) into a scaffold. It is reported that cells are more likely to be attached to small pores (< 40 μm) [46]. *In vivo* experiments showed that new bone was formed on porous hydroxyapatite with interconnected micropores on the walls of macropores while no bone formation was observed on porous hydroxyapatite with a smooth macropore wall [51]. The size of micropores in this experiment was reported to be in the 2 to 5 μm range [52]. It was believed that the mechanism for enhanced bone formation due to the micropores is enhanced surface area for protein adsorption [53]. Hence, more space is provided for cell attachment [54] and anchorage-like adhesion of bone precursor cells [51]. Surface roughness also affects osseointegration [55]. Osseointegration *in vivo* in rabbits was found to be encouraged in titanium implants with 18 μm rough surfaces (45%) compared to implants with 400 and 6 μm surface roughness (33 and 38%, respectively) [55]. Roughening the surface increases the non-polarity of a biomaterial surface, resulting in increased hydrophobicity that has been associated with the irreversible adhesion of high molecular weight proteins plasma fibrinogen and fibronectin [56]. *In vitro* experiments showed a greater amount of adhered cells on PMMAs with a rough surface than that on PMMAs with smooth surface [56]. Sul *et al.* [57] compared the osteoconductivity of the same material implants but with different surface morphologies. Implants were titanium screws with non-porous and porous oxide films. Porous surface implants had 12.7-24.4% porosity with pore size of few microns. All implants were implanted in rabbits and analyses were carried out at 6 weeks after implantation. Bone metal contact and newly formed bone indexes were found to be significantly higher in porous oxide surface implants than in non-porous surface implants. However, the variation in this study was

not only porosity of the surface of the implant but also the thickness, roughness, crystallinity and chemical composition of titanium oxide.

Thus, there is considerable evidence in the literature to conclude that the ideal scaffold for bone tissue engineering should possess an interconnecting porous structure with pore sizes in the range of 300 to 600 μm, pore interconnecting areas at least 100 μm wide and a surface exhibiting microporosity or some roughness.

1.1.4.3 Mechanical Strength

Patients have suffered from bone decease called osteoporosis believed to be caused by high stiffness orthopaedic metals [11, 12]. Osteoporosis is a bone decease making bone become more porous and leading to a reduction of amount of proximal bone stock or, in serious case, bone fracture [12]. Mechanism that high stiffness metals initiate osteoporosis is previously described in this report (see 1.1.3). Hence, ideal bone implant biomaterials should have mechanical properties as similar to natural bone as possible.

1.2 Magnesium-based biomaterials

1.2.1 Magnesium in the human body

Magnesium (Mg) is the fourth most abundant cation in the human body following Ca, K and Na. Adults have around 1 mol (or 24 g) of Mg of which nearly half is stored in muscle and tissues while the remainder is mostly stored in bone. Only around 1% of Mg is present in extracellular fluid [58-60]. Mg has been long known as a crucial element in the body playing an important role in many physiological and biological processes. Thus, it is crucial for the human body to control Mg concentrations in both intra- and

extracellular tissue. Absorption and excretion processes in the intestines (predominantly colon) and kidneys regulate Mg homeostasis [60-62]. To an extent, bone is also involved in Mg homeostasis. Bone is capable of rapidly releasing Mg into the plasma in the event of low extracellular Mg level or binding Mg to its surface if Mg concentrations become excessive [61].

The daily recommended intake of Mg has been recently revised. The revision brought age and, in women, the pregnancy status into account [61]. ~300-420 mg per day of Mg is the recommended intake for adults [61]. Deficiencies in Mg can lead to low Mg level in the plasma, resulting in illnesses such as anorexia, vomiting, lethargy, paresthesia, muscular cramps and irritability [62]. On the other hand, depression of the nervous system and muscle contractions are observed symptoms of excessive extracellular Mg levels [60].

Mg also plays several crucial roles in the intracellular system of the body. In terms of genomic stabilisation, Mg is required to regulate cell cycle (proliferation, differentiation and apoptosis), stabilise DNA's helix structure and stimulate DNA repair processes [63, 64]. Mg ions are transported between extra- and intracellular systems principally by diffusion process [62, 63]. Changes in intracellular Mg level are detectable when the extracellular Mg level is as low as 0.2 mmol/l. This indicates that intracellular Mg concentration is strictly controlled [61].

Mg is one of the crucial constituent ions in bone apatite [19, 26]. Table 1.1 contains information of chemical composition of bone apatite derived from literatures. A substitution of the constituent ions happens in the crystals of apatite and not on the

surface [19]. For example, Mg is capable of replacing calcium ion making the structure of apatite contracted and less crystalline [26]. The latter effect of Mg substitution in apatite leads to a rise in solubility.

1.2.2 Biological properties of magnesium

1.2.2.1 Bioresorbability of Mg

Unlike others metallic biomaterials, Mg and its alloys are reported to be bioresorbable [13, 14, 65-70]. Mg was first introduced, as a metal plate, in bone fracture fixing application by Lambotte in 1907. The result was unsuccessful as Mg completely corroded in only 8 days post-operation with generation of gas [68, 71]. Nevertheless, further attempts were made to use Mg and its alloys. Seelig [69] subcutaneously implanted chemically "pure" Mg strips in rabbits and dogs. This work also experienced a physiological reaction which involved the liberation of gas and a forming of Mg salt [13]. Recent *in vitro* analysis confirmed that the released gas is H_2 and Mg salt which appears as a white sediment is $Mg(OH)_2$ [72]. The H_2 gas pocket forming under a patient's skin occurs as the gas is released at a rate greater than the surrounding tissues can absorb. This gas pocket together with the disintegration of Mg could be clearly observed two weeks after the operation. However, at a later stage both the gas pocket and the calcined Mg were completely absorbed, disappearing from the implantation site. The same event was observed in the orthopaedic surgery performed in later clinical applications [13]. Plates and screws made of Mg alloy (alloyed with cadmium for mechanical strength) were implanted in femur, humerus and antebrachium [13]. The fractured bone reunited smoothly without infection. The resorption rate of the Mg was low enough to allow the bone to be healed completely. It was thought that the liberated hydrogen gas, to some extent, actually accelerated the formation of new bone. Znamenskii [14] also noted a

reduction in time required for bone healing when Mg alloy plates were inserted into the marrow cavity of human femurs. It should be noted that the results from Troitskii and Tsitrin [13] and Znamenskii [14] were obtained from macrostructural scale investigation, (*e.g.* diagnoses and examinations by orthopaedic surgeons and X-ray photographs) and no laboratory results were provided in the reports to support or prove the observations made.

All *in vivo* and clinical experiments on bioresorbability of Mg mentioned above showed no signs of toxicity toward the issues. Thus, it appears that the most concern in using Mg in orthopaedic implants is the rapid corrosion of Mg that leads to the formation of a gas pocket. In general, the capsule of gas causes no harm although, in rare cases, excessive gas can cause irritation. If this occurs, it can be simply treated by needle or acupuncture [14].

1.2.2.2 Other physiological properties

Other physiological properties that need to be addressed include cytotoxicity, sensitisation, irritation, genotoxicity, implantation, chronic toxicity and carcinogenicity [4]. These biological properties are standardised by FDA and ISO to be the tests required prior a biomaterial being commercialised.

Recently, Li *et al.* [73] conducted a preliminary *in vitro* experiment on cytotoxicity of pure and alkali and heat-treated Mg to cultured femoral marrow cells of mice. The results after up to 72 hours immersion were positive as cell proliferation and viability could be observed and inhibition of cell growth was not observed. Nonetheless, further *in vivo*

studies were stated as being necessary before firm conclusions on the cytotoxicity of Mg can be drawn.

Mg showed no signs of genotoxicity according to the review by Hartwig [63] on physiological concentration (up to 20mM). In fact, Mg was shown to be an anti-genotoxic metal ion. For example, it is capable of inhibiting the break down of DNA strands induced by Ni. However, Mg is not capable of inhibiting all genotoxic metal ions as it appears to have a metal-specific function. At too high or too low than normal physiological Mg concentrations, a DNA destabilization caused by Mg was observed [74]. At appropriate physiological concentration, Mg stabilises DNA through the production of DNA repairing enzymes. The repair of DNA keeps mutation low and, hence, stabilises DNA. On the other hand, if the Mg concentration is too high, the destabilisation of DNA will be initiated in the form of bending or distortion of the DNA structure.

The carcinogenicity of Mg is closely related to genotoxicity although more complex [63, 74]. Mg is long known to be an anti-carcinogen [64]. Carcinogenic diseases are known to be related to chronic Mg deficiency as evidence in both animal model and human epidemiological observations. Nevertheless, recent studies have emphasised concern of Mg supplementation on tumour growth acceleration. Mg appears to protect the tumour in the early stages of growth but promotes the growth of the tumour in later stages. Also, DNA destabilisation and degradation triggered by inappropriate Mg concentration is related to cancer formation in later stages. The relationship between Mg and carcinogenicity needs further clarification due to the complexity of its role in the human cell, enzyme and DNA [63, 64, 74].

Mg has been used in medical therapy with rare case of toxicity involved if patient has a healthy renal system [62]. However, at very high concentrations of Mg in the plasma, symptoms such as hyporeflexia, muscular paralysis, respiratory arrest or cardiac arrest can occur. With lower plasma Mg concentrations, minor illnesses can develop, such as warm flushed skin, dry mouth, vomiting, nausea, hypotension and drowsiness. These are acute effects, rather than chronic, where Mg is administered rectally or orally and the symptoms of an overdose show within only a few hours [62]. As far as the information found in literature, no case of Mg chronic toxicity has been reported. This might be due to the fact that excessive Mg ions in the blood stream are excreted by the renal system in a relatively short time [75].

Mg has been known for some time to be a bacteriolysis or an anti-bacterial substance. Work performed by Delbe (as cited in Znamenskii [14]) showed that salts of Mg can increase the performance of phagocytosis process up to 75% by increasing both the amount of leukocyte and the intensity of phagocytosis. Hence, the resistance to trauma, infection, and narcosis of tissue can be improved. Seelig also demonstrated that Mg was effective in retarding the growth of typhoid bacilli [69].

Osteoblastic cells initiate the bone formation process. Osteoblasts secrete a substance that later becomes the bone matrix. If osteoblasts fail to adhere to the surface of implanted biomaterials, cell proliferation, differentiation and mineralisation will not proceed and new bone cannot form on the surface of the biomaterial. Osteoblast adhesion is, therefore, an important issue for successful biomaterials [76]. *In vitro* [76] and *in vivo* [77] experiments have shown that substitution of the Mg ion in a carbonate-substituted hydroxyapatite (Mg-CO_3-HAp) greatly increases the amount of adhered osteoblast cells.

The new bone formed was also clearly higher in density on the implanted Mg-CO_3-HAp. Integrins are the cell membrane proteins that adhere to the surface of the implant material and control the cellular response of surrounding tissue to the implant [78]. It is believed that Mg^{2+} is preferred over Ca^{2+} by most adhesion proteins such as integrins [76]. Thus, Mg^{2+}-containing HAp attracts more cells than HA releasing Ca^{2+} when dissolved in the human body fluid. Furthermore, Mg^{2+}-doped HAp was found to enhance the osteoblast differentiation process compared to undoped HAp [79].

Revell *et al.* [80] conducted ion beam implantation of Mg ions at the surface of hydroxyapatite-coated titanium samples. The depth of penetration was less than 60 nm, implying that the ions did not incorporate into HA structure, remaining isolated at the HA surface. Mechanical tests for interfacial shear strength were carried out at six weeks after implantation, showing significantly stronger bonding between implant and bone for the Mg-doped samples compared with the un-doped samples. There have been reports, as cited by Okuma [58] showing a relationship between dietary deficiencies in Mg and reduction of bone strength as studied in rats. These effects may relate to the fact that Mg affects the absorption and transportation of Ca and K – two major constituents of bone apatite.

On the contrary, Serre *et al.* [81] carried out a study showing that Mg-substituted collagen-apatite biomaterials exhibited decreased osteoinduction, creating a toxic environment for bone cells and inhibiting bone matrix formation. However, the Mg levels used in their study (20 and 80 wt. %) were relatively high compared to the studies referred to above and higher than the actual physiological level of Mg. Thus, it appears

the substitution of Mg ions into biomaterials can introduce either positive or negative effects depending on the concentration.

1.2.3 Mechanical properties of Mg scaffold for orthopaedic application

Figure 1.6 illustrates a compressive stress-strain curve characteristic of cellular materials, showing three distinguishable regions. The first region is an elastic region where a straight line is observed. In the second region plastic deformation and cell wall collapse take place. There is much space between the cells so that large deformation is possible without an increase in applied load. Thus, second region exhibits a characteristic plateau. In the third and final region, the collapsed cells are further pressed together, leading to a steep increase in stress.

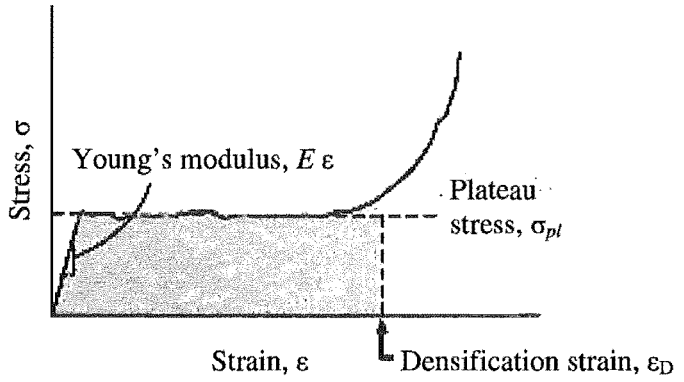

Figure 1.6 Typical compressive stress-strain curves of cancellous cellular structure [82].

The mechanical properties and behaviour of cellular materials depend heavily on their relative density and empirical models have been constructed based on this property [18, 23, 82]. The compressive strength and elastic modulus of Mg foam are determined using the mathematical models as listed in Table 1.4 under assumption of maximum relative density and model constant at 0.7 and 1, respectively, with 0.2% compressive yield

strength of 21 MPa. The mechanical properties of Mg foam compared with those of natural bone and bulk Mg are shown in Figure 1.7. The predicted mechanical properties of Mg foam are obviously closer to those of natural bone compared with current metallic biomaterials (Figure 1.5), making Mg foam a more mechanically suitable orthopaedic biomaterial.

Table 1.4 Models for estimation of mechanical properties of cellular materials.

Mechanical Property	**Open-cell foam (Ashby [82])**
Elastic modulus, E	$E_f = (0.1 \text{ to } 4)E_s\left(\frac{\rho_f}{\rho_s}\right)^2$
Compressive strength, σ_c	$\sigma_{c,f} = (0.1 \text{ to } 1)\sigma_{c,s}\left(\frac{\rho_f}{\rho_s}\right)^{3/2}$

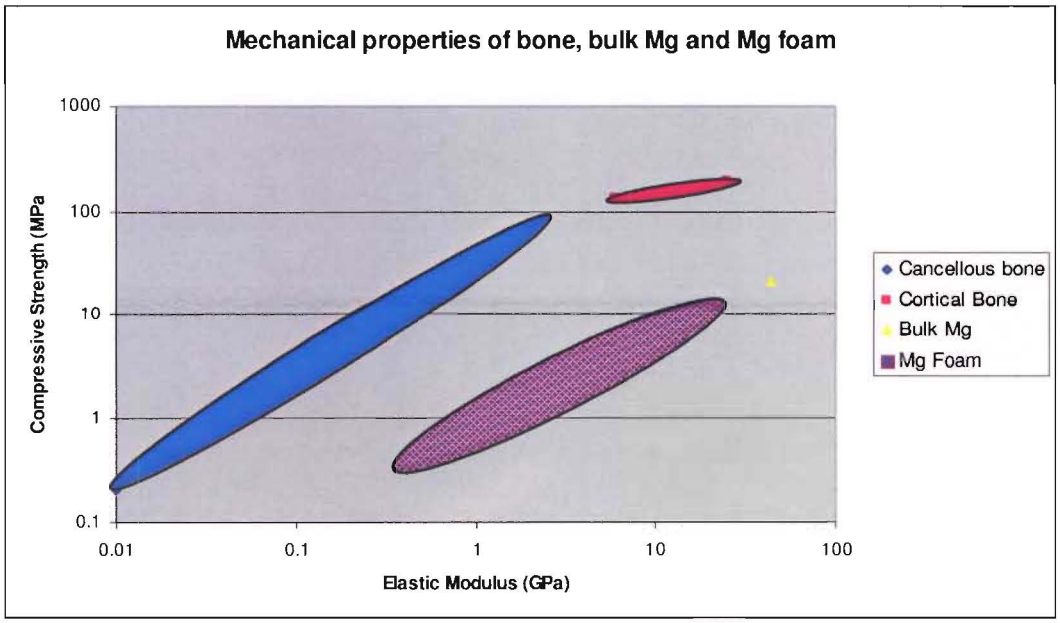

Figure 1.7 Comparison of predicted mechanical properties of Mg foam compared to natural bone and bulk form of Mg.

1.3 Fabrication of Mg scaffolds

The processing route of metal matrix composites can be broadly categorised into one of two different categories depending on the state of matrix material *i.e.* solid and liquid state [83]. Table 1.5 provides an overview of the main cellular foam technologies [82, 84].

Table 1.5 Summary of manufacturing method - advantages and limitations. Summarised from Banhart [84] and Ashby *et al.* [82].

Method	Short description	Advantages	Limitations
Direct gas injection into metal melt	Fine bubbles are generated in molten metal by means of gas injecting through the rotating propeller. Fine reinforcement powders can be added to the melt to increase liquid viscosity.	• High porosity ranges from 80 to 98%. • Feasible for large and continuous production line.	• Large foam size (3-25 mm.). • Closed-cell pore. • Brittleness of pore wall introduced by the reinforcing materials.
Gas-releasing agent into metal melt	Agent that releases gas when it is heated is added to the melt at temperature lower than its decomposition point. The whole melt is then further heated to a temperature above the decomposition point of agent material. The metal melt is thickened to ensure the produced gas will remain in the melt until it solidifies.	• More homogeneous pore structure than direct gas injection. • Porosity or density range is broad.	• Relatively large foam size (>0.5 mm) • Closed-cell pore.
Gas-solid eutectic solidification	Metal is heated under high pressure (<50 atm) of hydrogen atmosphere. The temperature is then lowered to reach eutectic point where hydrogen gas is formed and kept in the melt until metal solidifies.	• Employed with only metal that has eutectic system with hydrogen gas. • Autoclave or pressure vessel is required.	• Pore morphology is oriented along a direction of liquid metal solidification and thus there is no pore network. • Pore size distribution is non-uniform. Size range of pore is broad from 10 μm up to 10 mm. • Relatively costly process as too many process variables need to be closely controlled.

Method	Short description	Advantages	Limitations
Metal powder with gas release agent	Compact composite fabricated from mixture of metal powder and blowing agent is heated at temperature near the melting point of the metal. Blowing agent decomposes and releases gas resulting in pores in metal matrix. The gas also forces the matrix to expand.	• Pore size distribution is relatively uniform if the expansion of the compact is confined to be lower than the full expansion point.	• Closed-cell pore.
Metal powder with space-holding particle	Mixture of metal powder and space-holding particle is cold or hot compacted. The space-holding particles can be removed by thermal treatment or leaching. The porous metal can be further sintered at elevated temperature to obtain strong bonding between metal particles and, thus, better mechanical properties of the porous metal.	• Control over porosity and pore size and shape by selection of amount, shape and size of space-holding particles.	• Difficulty to completely remove space-holding particle.
Casting in porous template	Liquid metal is poured into porous template previously fabricated. Template material is subsequently removed by means of heat treatment or leaching in water or other suitable solvents. The structure of pore replicates that of template used.	• Close control over porosity and the size, shape and morphology of pore by the selection of preform. • Open-pore structure and interconnected-pore network. • Near-net-shape sample can be easily obtained. • Porous network.	• Template needs to be previously fabricated. • Incomplete liquid metal filling into template is not unusual. • Difficulties from removing template material without too much damaging metal matrix. • Wetting might be an issue and vacuum-, gas-, or mechanically-induced force may be required.

Method	Short description	Advantages	Limitations
Gas entrapment technique	Loose compact metal powder is first evacuated then backfilled with overpressure gas. The compact is then heated under pressure (hot isostatic pressure, HIP) resulting in pore with pressured gas in it. At this stage, the compact porosity is very low (<2%). Hot rolling is introduced to increase the uniformity of pore distribution. Finally, the near-net-shape metal foam can be obtained by performing an annealing treatment during where gas slowly expands by creep of surrounding metal and reaches an equilibrium state.	• Sandwich structure can be obtained without applying adhesive substance.	• Relatively low porosity. Theoretical maximum is only 50%. • Unconnected-pore structure. • Too many steps.
Metal deposition on porous template	Metal deposit on open-cell porous template by means of chemical vapour deposition (CVD), or electrodeposition or evaporation. The template material is subsequently removed by mean of heating resulting in a network of hollow metal struts.	• Wide rage of pore size, i.e. from few hundreds micron to few millimetres. • Highly porous structure is possible, i.e. 95-98% porosity. • Control over structure of final metal foam by selecting the structure of template.	• Limited to only pure elements as the difficulty of deposition of alloys.
Metallic hollow sphere	Polymer sphere is first coated by metal by means of, for example, chemical or electrical deposition. Metal-coated polymer sphere is then fabricated into desired shape and sintered. Polymer is removed during sintering step. Metal hollow sphere can be alternatively and directly prepared by atomisation technique.	• Uniform structure • Control over the morphology of porous structure by the control of sphere size. • Low density and wide range of structural pore size.	• Complexity of hollow sphere fabrication.

1.3.1 Previous Productions of Mg foam

Several production methods have proven to be able to produce metal foam although only a few are suited to fabrication of porous Mg [84]. Mg scaffolds have been successfully produced by both liquid- and solid-state production methods [85-88]. Liquid-state processing can be carried out by injecting liquid Mg with high velocity into a 2 cavity permanent mould (Figure 1.8). The first cavity (mixing cavity (2)) contains a blowing agent powder (MgH_2) that will mix with the molten Mg before entering into second cavity (part forming cavity (3)) [85]. Mg foam produced from this process is illustrated in Figure 1.8. The foam has closed-cell pores with a non-uniform pore structure throughout the sample. Small pores tend to be observed near the outer surface whilst bigger pores congregate at the centre of the casting.

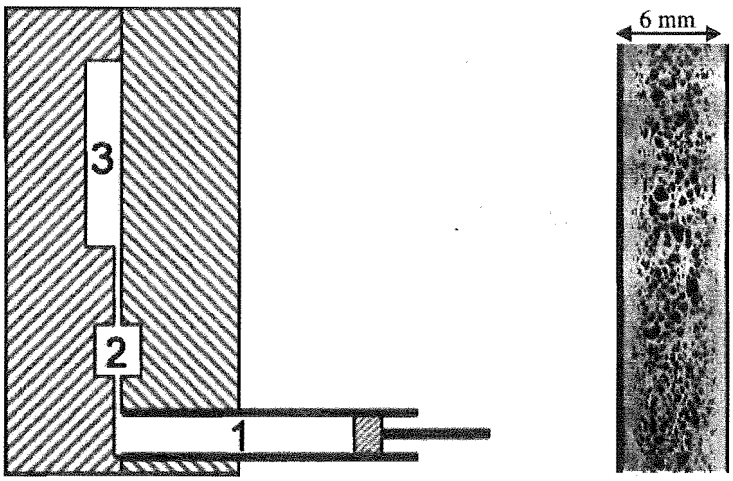

Figure 1.8 Cross-section view of a) permanent injection mould and b) resultant Mg foam.

Casting using a porous template technique has also been employed to manufacture Mg foam [88]. A porous template is pre-fabricated by pouring a slurry of plaster into an open cell polyurethane (PU) foam. Once the plaster sets the PU foam is removed by firing at 500°C, resulting in a porous plaster template with a pore structure resembling that of the

PU foam. The porous plaster template is then infiltrated with molten Mg *via* a vacuum-induced pressure. The plaster is then removed from the Mg by means of water spraying. The process is illustrated schematically in Figure 1.9. Optical micrographs of the initial PU foam and resultant Mg foam are shown in Figure 1.10, demonstrating the correspondence between the two structures [88]. Thus, the microstructure of the metal foam can be anticipated based on the structure of the polymer foam. However, the casting mould needs to be carefully designed to ensure a vacuum can be applied during casting.

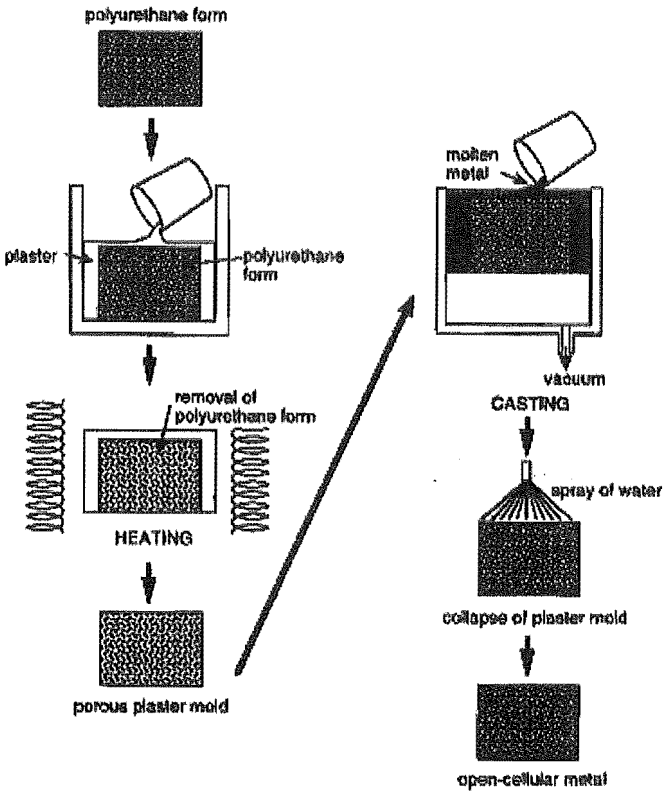

Figure 1.9 A schematic diagram of producing Mg foam by casting in porous template [88].

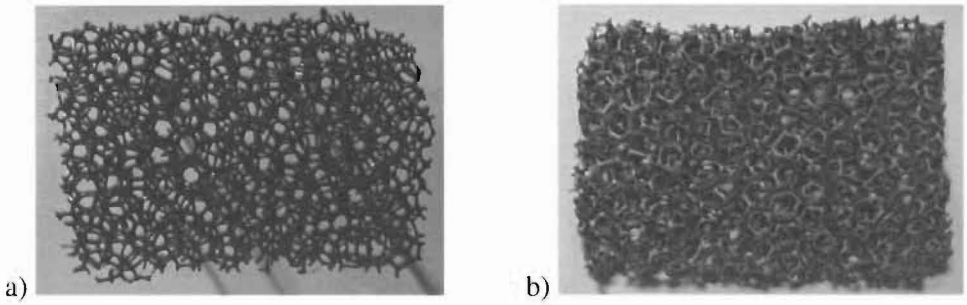

Figure 1.10 Photographs of a) polyurethane foam and b) resultant Mg foam

A hollow sphere technique was also shown to be possible for making Mg foam [89]. Alumina hollow spheres are stacked in a die underneath where Mg is melted in the crucible. Once the Mg completely melts, the whole furnace chamber is evacuated to a pressure level of 100 mbar and the die is lowered until the die inlet is immersed in liquid Mg. Ar gas is then backfilled into the chamber creating an internal pressure of 500 mbar that forces liquid Mg to infiltrate into the alumina hollow spheres. Liquid Mg is allowed to infiltrate for 2 min then the die is raised. A schematic of this process is shown in Figure 1.11 [89]. The Mg foam has a pore size similar to the hollow spheres.

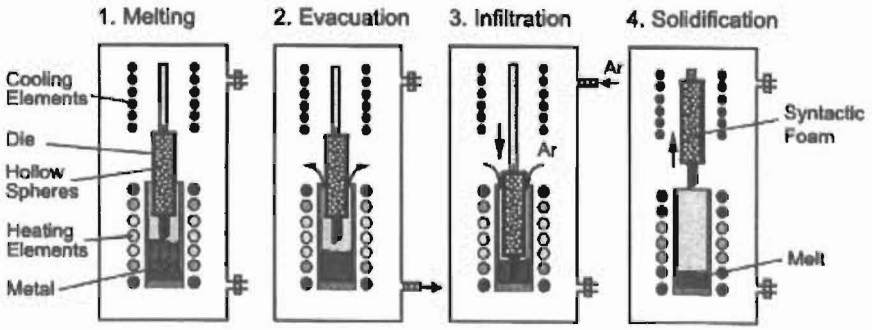

Figure 1.11 Schematic diagram of production method of Mg foam using hollow spheres.

Mg foam can be also be fabricated *via* a powder metallurgy route [86]. Mg powder is mixed with spacer particles and then pressed to obtain a green body. The spacer material must be soluble [90] or have a decomposition temperature much lower than the sintering temperature of the matrix metal [86]. A ∅45-600 μm carbamide or urea ($CO(NH_2)_2$) has been selected as a spacer material for production of Mg foam [86]. The green compact of Mg/carbamide was heat treated at 200°C for 5 hrs to burn off carbamide and the remaining Mg was then sintered at 500°C for 2 hrs. A schematic diagram of this production route is shown in Figure 1.12 [86].

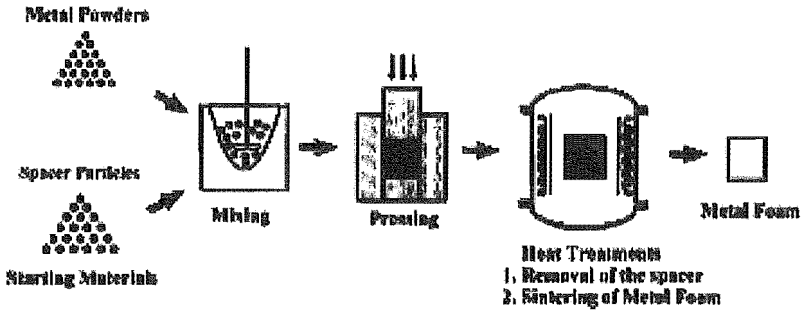

Figure 1.12 Powder metallurgy route using spacer particles.

The porosity of the Mg foams varied from 35% to 55% [86, 87]. Pore sizes were in the range of several hundreds microns which agrees well with the size of urea particles used. There were also micropores present in the walls of the macropores of the foam. The micropores are thought to be caused by shrinkage of Mg during sintering. This route allows relatively accurate control over the final pore size. However, one difficulty with this foaming technique is completely removing all of the spacer particles. The complete removal of urea is possible only if the content of spacer particle is sufficiently high to form an interconnected network [84]. Peaks corresponding to C and N in EDS analysis provided some evidence of residual carbamide spacer particles at the surface of the pore

wall in 45% porosity Mg foam [87, 91]. Urea is a form of body waste; thus, residual carbamide is likely to cause adverse effects in the body if introduced *via* a biomaterial. Another concern in this fabrication route is the high reactivity of Mg, especially in a fine powder form. The formation of an oxide film on Mg particles is unavoidable, creating a barrier that makes the sintering of the Mg particles very difficult. This oxide film can be broken down by ball mill the powder. Since Mg is a highly reactive metal, new oxide film instantly forms on the surface of Mg particles. Therefore, the ball milling process and each subsequent step in the process must be performed under a protective atmosphere such as high purity argon. This makes the powder metallurgy route an expensive and complicated process for making porous Mg.

All of the above processes for fabricating a Mg foam have both advantages and disadvantages. An economically route is required for the fabrication of Mg foam with design characteristics demanded by an orthopaedic biomaterial.

1.3.2 Liquid infiltration process

Based on the expense and problems associated with powder metallurgy of Mg, it would appear the most suitable production method for Mg foam is via a liquid infiltration process. In this technique, a porous template is pre-fabricated allowing control over the final structure of the Mg foam. The following sections focus on the most important process parameters for infiltration of liquid metal into such a porous template.

1.3.2.1 Contact angle and wettability

In ceramic-reinforced metal matrix composites, wettability is a major concern as ceramics are not generally wetted well by liquid metals, resulting in a need of external pressure during infiltration. Figure 1.13 demonstrates the behaviour of a liquid metal when dropped on solid surface. The contact angle and all three relevant surface energies are also defined. The subscripts used to distinguish each of the surface energies refer to the solid (S), vapour (V) and liquid (L). The surface energy of the liquid, γ_{LV}, is also referred to as *surface tension* [92]. In the equilibrium state, the relationship between the surface energies and contact angle is described by Young's equation [93]:

$$\gamma_{SV} = \gamma_{SL} + \gamma_{LV}\cos\theta \qquad 1.1$$

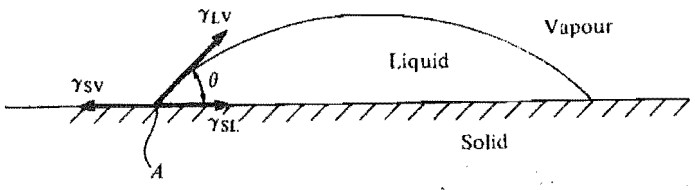

Figure 1.13 Contact angle (θ) and three surface energies (γ_{SV}, γ_{LV} and γ_{SL}) for a liquid drop on a solid surface [93].

Principally, ceramic-metal system behaves in the way that total system energy is minimised. Thus, in the system where γ_{SL} is high, the liquid tend to form a ball-like shape in order to minimise system energy by reducing the area of the solid-liquid interface as shown in Figure 1.13a [92]. In this case, a large contact angle is observed and the system is considered to be non-wetting. On the contrary, if γ_{SV} is large then the surface tension of liquid and solid-liquid interface energy is overcome and the liquid spreads out over the solid surface. This reduces the solid surface and increases the solid-

liquid interfacial area, thus, reducing the overall system energy. As liquid spreads over the surface, a small contact angle is observed as shown in Figure 1.14b.

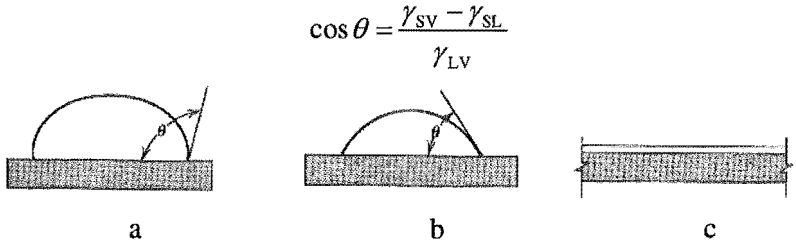

Figure 1.14 The difference in contact angle of (a) non-wetting system ($\theta > 90°$), (b) wetting system ($\theta < 90°$), and (c) complete wetting system ($\theta = 0°$).

1.3.2.2 Threshold pressure for infiltration process

Generally, an external force is required during infiltration processes used to fabricate metal-ceramic composites. Numerous attempts have been carried out to develop mathematical equations to estimate the level of pressure required for complete infiltration of the ceramic fibres or particles that constitute the preform or template as it is referred to here [83, 94-98]. The most important characteristics of the preform are the average fibre/particle size, pore diameter, pore shape, density or volume fraction and specific surface area.

The simplest mathematical model to determine this pressure, also known as threshold pressure, is Kevin's equation:

$$\Delta P = \gamma_{LV}\left(\frac{1}{r_1} + \frac{1}{r_2}\right) \qquad 1.2$$

where γ_{LV} is the surface tension of the liquid while r_1 and r_2 are the principal radii of curvatures at the liquid front as shown in Figure 1.15 [83].

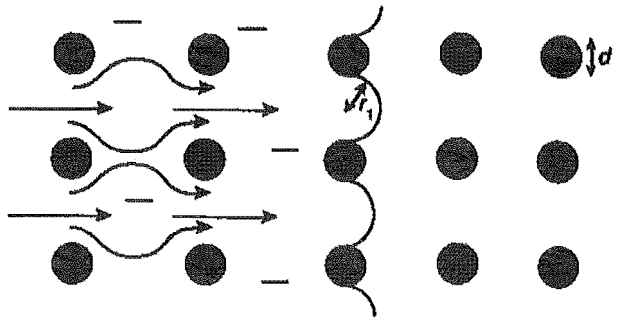

Figure 1.15 Illustration of the infiltration front of metal flowing through a bundle of reinforcement fibres.

However, Kevin's equation ignores a critical factor in the liquid/solid system – the contact angle (θ). More recent mathematical equations combine more variables derived from the characteristics of the template [95, 96]. For example, the Washburn equation [99]:

$$\Delta P = (2\gamma_{LV}\cos\theta)/r \tag{1.3}$$

where, r is pore or capillary radius, or

$$\Delta P = (\gamma_{SL} - \gamma_{SV})S_f \tag{1.4}$$

where, S_f is the fibre or template surface which can be estimated by

$$S_f = \frac{6V_f}{(1-V_f)d_f} \tag{1.5}$$

where, V_f is the volume fraction of particle template and d_f is the diameter of the particles [96]. Substitution of Eq. 1.4 by Eq. 1.1 and 1.5 will lead to:

$$\Delta P = \frac{-6V_f\gamma_{LV}\cos\theta}{(1-V_f)d_f} \tag{1.6}$$

Predictions of the required threshold pressure during infiltration were calculated by varying the contact angles and template conditions since θ of liquid Mg on a NaCl

substrate was unknown (Figure 1.16-1.17). Note that in Figure 1.16 the Washburn equation was modified by inserting a negative sign in the equation in order to make the interpretation and comparison easier to follow. V_f used in the Mortensen & Cornie model (Figure 1.17) was estimated to be 60% based on the average density of a random loose packing of particles (*i.e.* 54-62%) [100]. Spontaneous infiltration is possible for a given system when the resulting threshold pressure is zero or negative. Spontaneous infiltration does not require an external force so that infiltration is need only be assisted by the force of gravity on the liquid metal. On the other hand, external pressure is required if the threshold pressure is predicted to be positive.

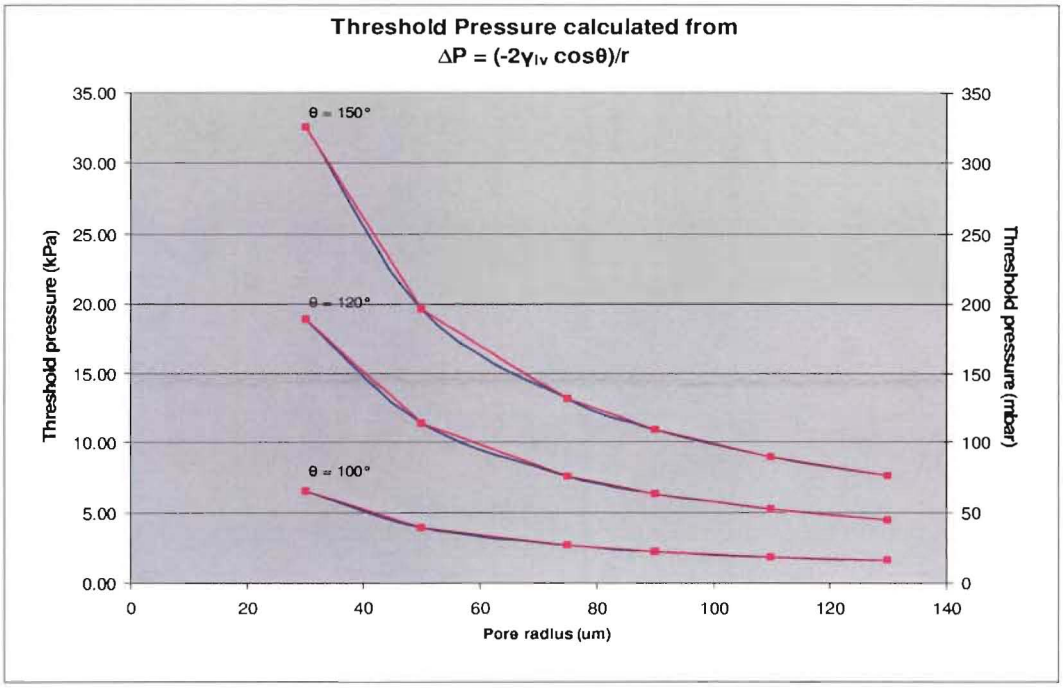

Figure 1.16 Threshold pressure calculated by Washburn equation.

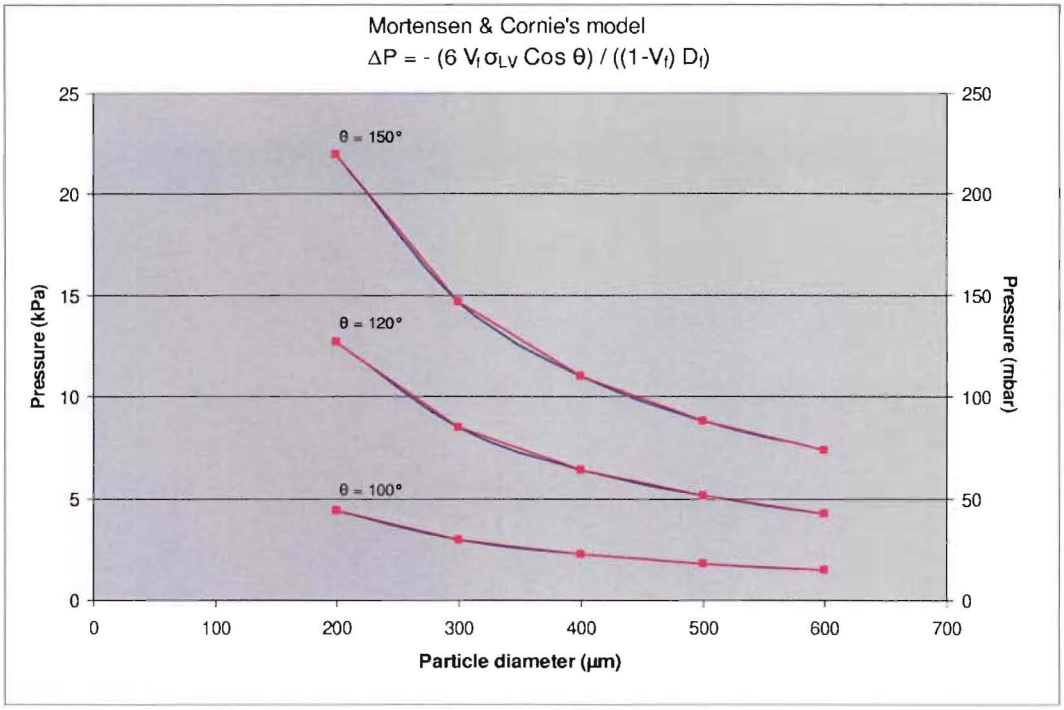

Figure 1.17 Estimated threshold pressures to infiltrate Mg liquid into templates with various particle sizes.

As was discussed, the particle size preferred in a biomedical scaffold is in the range of 300-600 μm. Assuming that V_f is 60% for a random loose green compact [100] and θ of the system is 150°, the required threshold pressure is ~150 mbar according to the Mortensen & Cornie model. The smallest pore size needs to be known in order to use the Washburn equation. The smallest pore diameter is ~63 μm for three ∅ 400 μm particles contacting. Although in general the shape and size of particles change during sintering, the main sintering mechanism of salt with a particle size >150 μm is evaporation-condensation – a sintering mechanism that does not lead to extensive densification or shrinkage [101, 102]. Thus, changes in the size and shape of pores is expected to be minor during sintering of NaCl. Using these assumptions, the Washburn equation estimates a threshold pressure of 320 mbar, assuming θ is 150° – *i.e.* twice that predicted by the Mortensen & Cornie model.

1.3.2.3 Differential Pressure

In a non-wetting system, liquid metal can infiltrate into the small pores of a template if there is a difference of pressure inside template and that externally pushing the liquid. Therefore, the threshold pressure can also be applied in the form of a differential in pressure between the template and liquid metal. With this in mind, the idea of vacuum-initiated differential pressure was first trialled by Cochran [103]. Principally, the process starts with evacuating the crucible in which the template and metal ingots are located so that the pressure in the template reaches a low level. The metal is made molten so that it completely covers the template. Therefore, the pressure inside the porous template is kept at a low level while it is isolated by the surrounding liquid metal. The pressure inside the furnace chamber is then brought back to atmospheric level. The pressure differential obtained at this stage acts to push the liquid metal into template. Assembly of the crucible, template and ingots is shown in Figure 1.18.

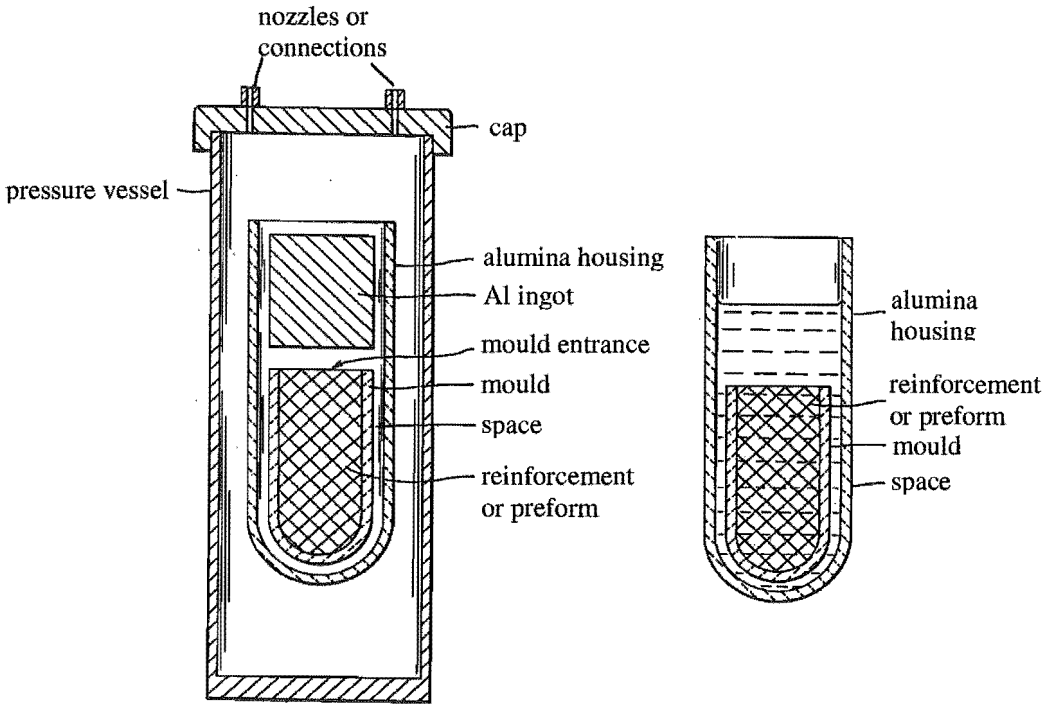

Figure 1.18 Schematic diagram showing how to prepare the crucible for infiltration process with pressure differential.

This method developed by Cochran has been adopted and further developed such that greater control is possible over casting parameters [104]. An example is shown in Figure 1.19 where a reinforcement or template is heated in the mould while the metal ingots are being melted in the crucible underneath. The metal is melted under vacuum atmosphere until fully molten then gas from outside the vessel is then allowed to re-enter providing a pressure that drives the melt to flow up into the mould. Another advantage of manufacturing under vacuum is that trapped air pockets that can occur in turbulent high pressure processes are minimised. Parts manufactured by conventional die-casting may contain 10-40 cm^3 of trapped air per 100g. In contrast, parts fabricated in vacuum die-casting (pressures less than 100 mbar) show no air pockets with improvements in physical and mechanical properties [105].

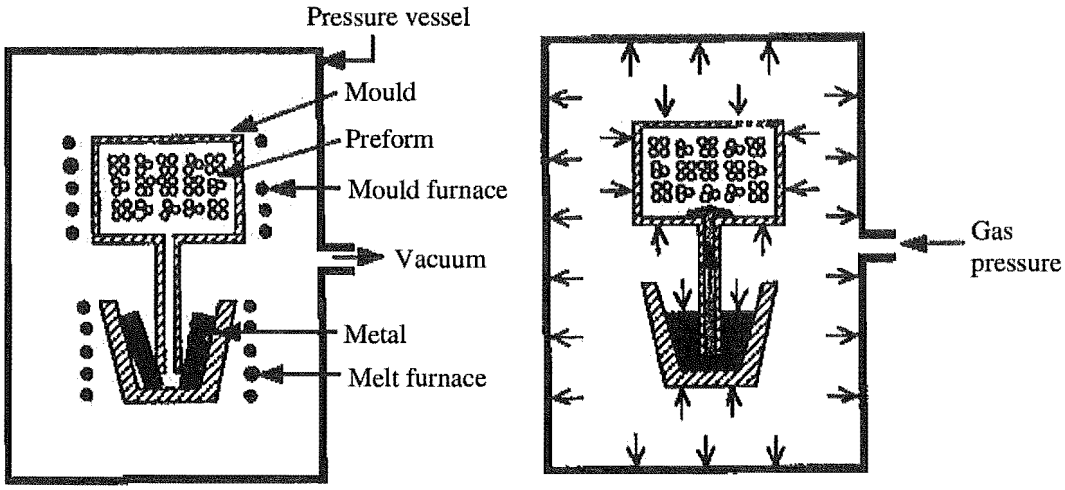

Figure 1.19 Schematic diagram of the general production equipment for vacuum infiltration.

According to these approximations, the threshold pressure is ~150 mbar for the Mg foam of interest in this work. This value is relatively low compared to atmospheric pressure (1,013 mbar) so that only small differential pressures are predicted to be required.

1.3.2.4 Selection of template materials

Material capable of being used as template in Mg infiltration process must be able to withstand temperature at melting point of Mg (*i.e.* 650°C) or even higher if superheating of liquid metal is needed (*i.e.* >700°C). The material must be easily leached from Mg after infiltration is complete. Sodium chloride (NaCl) is a cheap salt, abundantly obtainable by drying the brine, having a melting point of 801°C which is sufficiently high even if superheating has to be operated. Salt was formerly used as a template in Al casting to fabricate Al foam [106] providing a potential that salt can be also used in Mg casting. Fluoride salt with high melting point, *viz.* NaF, is potentially toxic from F_2 gas

that might have been released during casting process. NaCl is also water soluble and supposed to be easily removed from Mg foam. Unlike urea, NaCl is not toxic so the residual, if any, is expected to cause human tissue no harm.

1.4 Objectives and Scope

Millions of people have undergone orthopaedic surgery around the world. The number of hip arthroplasty in UK alone is estimated to be around 40,000 annually while that in the US is greater than 600,000. The number is thought to be double this when the number of knee arthroplasty is combined. Furthermore the figure is likely to increase owing to longer life expectancies [1, 12].

The industrial application of Mg has increased rapidly in the last 10 years. The increased usage of Mg is due to it being lightweight, and having high specific stiffness and strength. There has been interest in using Mg as a biomaterial for bone replacement as it is biocompatible and bioresorbable. Moreover, its mechanical properties are closer to natural bone compared with other metallic materials used as biomaterial implants (e.g. Ti alloys, Co-Cr alloys).

From literatures, it seems that Mg is a high profile material for bone implant application. It is bioresorbable metal that can be fabricated in a porous structure which promisingly has mechanical properties, *i.e.* modulus and compressive strength, closer to human natural bone compared to conventional metals.

The primary objective of this research is, thus, to investigate manufacturing routes for fabrication of Mg foam with structure required in tissue engineering and bone implant applications. The present research aims to deliver the manufacturing route that is not only feasible but also economical.

2. Experimental procedure

2.1 Salt template

The material chosen for producing a template was NaCl as it has melting point of 801°C which is considerably higher than the melting point of Mg (650°C). Common salt is also highly soluble in water which should ease the leaching of the template. Commercial table salt was sieved to obtain particles in the 422-599 μm size range. Salt particles are naturally angular in shape. Salt templates were prepared by sintering the salt particles in mould made of refractory material (Fibre Frax). The sintering step was carried out at 799°C for various sintering times, i.e. 2, 3, 5, 8, 12 and 15 hours, to determine the shortest sintering time required to provide a sufficiently strong template that could be handled. The weight and dimensions of the salt were measured to determine the volume fraction of template. The balance with 10^{-4}g resolution and the digital vernier calliper were used to measure the weight and the size respectively. Microstructural analysis of salt template by SEM and μ-CT was carried out on selected salt template. Salt templates had to be gold coated prior to SEM. During SEM analysis, the voltage was set at as low as 4kV to avoid the electrical charge building up on the surface of the sample. 2D micrographs obtained from SEM revealed the surface, topology and particle neck region of salt template. In order to obtain 3D structural images of salt template, software called Image J, 1.34s version, was used to construct 3D images from 2D images obtained from μ-CT. Volume fraction and porosity of the template were calculated from 3D images using built-in plugin of Image J called voxel counter and the obtained values were then compared to those obtained from conventional method. Compressive strength of salt

template was performed on 10x10x20 mm sample using MTS 858 Table Top System with small load of 10 kN and crosshead speed of 1 mm/min.

2.2 Mould preparation

A Mg ingot was firstly pre-fabricated by machining into a cup and placed at the base of a steel crucible (Figure 2.1). The salt template was placed inside the Mg cup. The Mg cup was used to assist with absorbing the heat generated in the steel crucible and to ensure that the template was completely surrounded by molten Mg upon melting of the Mg cup. Thus, liquid Mg fully surrounds and makes contact with the side and bottom surfaces of the NaCl template. It was necessary to fix the NaCl template in position *via* a bolt and steel rod at the base of the Mg cup otherwise its low-density results in the template floating to the top of the Mg melt. The other end of the rod was attached with a steel strip. The steel strip was fixed to the crucible by small nuts or wire. The melt temperature was measured using a K-type thermocouple inserted inside a thin sealed steel tube that was placed inside the steel crucible (not shown in Figure 2.1). Finally, small pieces of Mg ingot were placed on top of the NaCl template. The steel crucible and its contents were then dried in a furnace at 150°C for 2-3 hours just prior to casting.

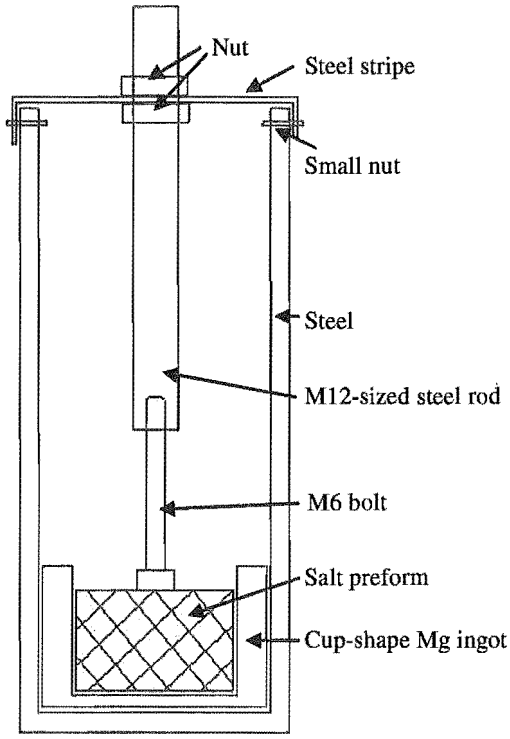

Figure 2.1 Mould design for Mg infiltration into salt template

2.3 Casting and infiltration process

The steel crucible and contents was placed in the middle of the induction coil in the pressure chamber of the furnace. A protective atmosphere of N_2 was supplied *via* a glass funnel placed above the steel crucible (Fig. 2.2 a) at a flow rate of at least 1.7 l/min. The Mg ingots were fully melted under atmospheric pressure so that the salt template was fully immersed in liquid Mg. The melt was then superheated to 730°C and held for 5 min to allow oxides and/or impurities to float to the surface of the melt. This was followed by evacuation of the chamber to give a pressure of 400 mbar by applying vacuum for a few seconds and then removing the vacuum to allow N_2 gas to repressurise the chamber up to

atmospheric pressure (~1000 mbar). This process was then repeated to assist with the infiltration of the template.

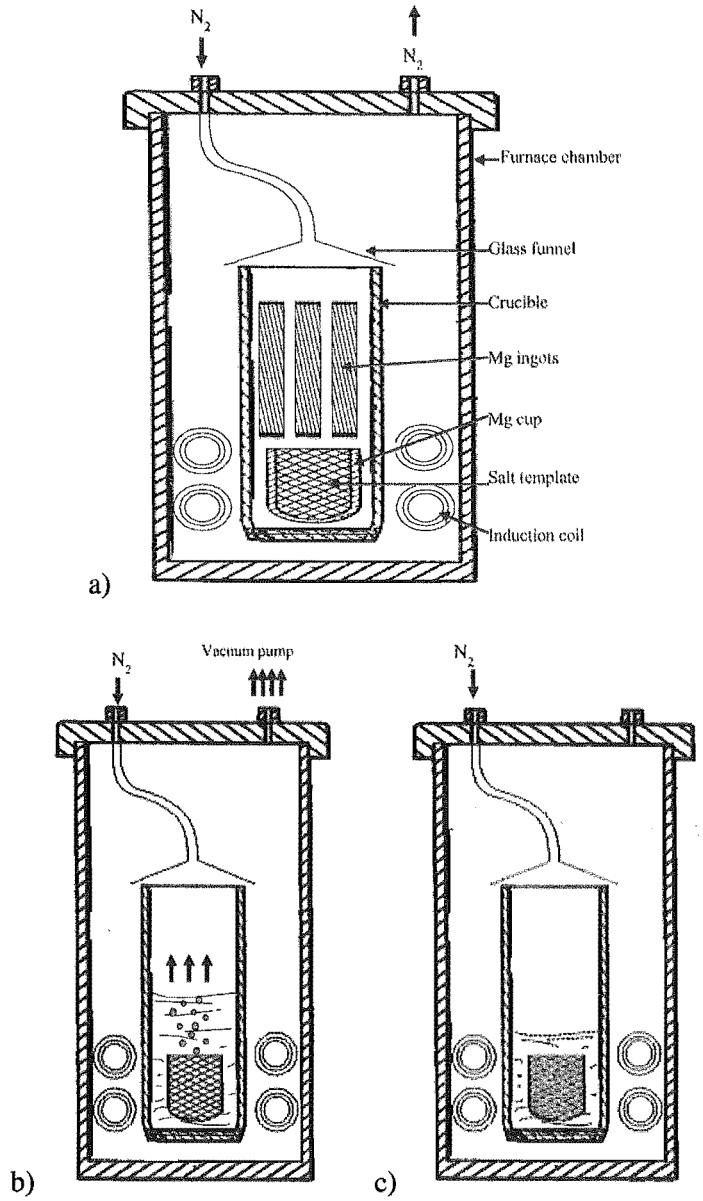

Figure 2.2 Schematic diagram of infiltration process employed in this project: a) setting up of the casting, b) evacuation step and c) N_2-pressurised infiltration.

The melt was then allowed to solidify by switching the induction furnace off. Once the temperature was below 600°C the flow rate of N_2 gas was reduced to 0.5 l/min and then stopped below 400°C. The resulting Mg-NaCl "composite" was cut to remove any solid Mg skin so as to expose the porous structure. The sodium hydroxide granules were added in water until the pH of solution > 11.5. Base solution was exploited due to its ability to stabilise the protective hydroxide layer of Mg [107, 108]. The porous samples were finally immersed in a solution.

2.4 Microstructural Characterisation of Mg foam

SEM technique was employed to analyse microstructure of as cast Mg-NaCl composite and Mg foam. The voltage of 4kV Samples of Mg-NaCl composite were gold coated in 3 directions, with 30 secs in each direction, prior an analysis to make it conductive. 2D micrographs obtained from SEM revealed the interfacial region, in case of Mg-NaCl composite, and the shape and size of pore, in case Mg foam. The surface and topology of pores in Mg foam were also illustrated.

In order to obtain 3D structural images of Mg foam, μ-CT technique was used. Thin sample of Mg foam was mounted and images were taken with a Skyscan 1072 using an unfiltered tungsten X-ray source operated at 80kV and 120 μA. Projection images were then converted to tomograms that subsequently used to construct 3D images with software called Image J. Volume fraction and porosity of Mg foam were calculated using Image J and compared with that obtain from conventional method.

2.5 Mechanical Testing of Mg foam

Mg foam samples 8 mm in diameter and 13 mm in height were prepared for compressive strength tests to comply with guidelines by Ashby *et al.* [82]. It is recommended that the minimum dimension is at least 7 times the average pore size and that the height-to-thickness ratio of the sample is greater than 1.5. Compressive strength test was performed using MTS 858 Table Top System with small load of 10 kN and crosshead speed of 1 mm/min.

3. Experimental results and discussion

3.1 NaCl template – Characteristics and Properties

3.1.1 Microstructural characterisation

Figure 3.1 a-f illustrate 3-hour sintered salt template showing a small fused area, as shown in Figure 3.1 f, and pores on the surface of salt particles, as revealed in Figure 3.1 d-f. These small pores of few ten microns in size emerged after the sintering step as evident by the SEM micrographs of salt particles prior to sintering shown in Figure 3.2 a-d. This might be a result of evaporation that occurs during sintering. When compare Figure 3.1 e and 3.2 c that have the same magnification, it is clearly seen that the step-like surface on the salt particle almost completely disappeared after sintering. The size and shape of the salt particles after sintering, however, was not altered significantly, as shown in Figure 3.1 b and 3.2 a, presumably due to the short sintering times used.

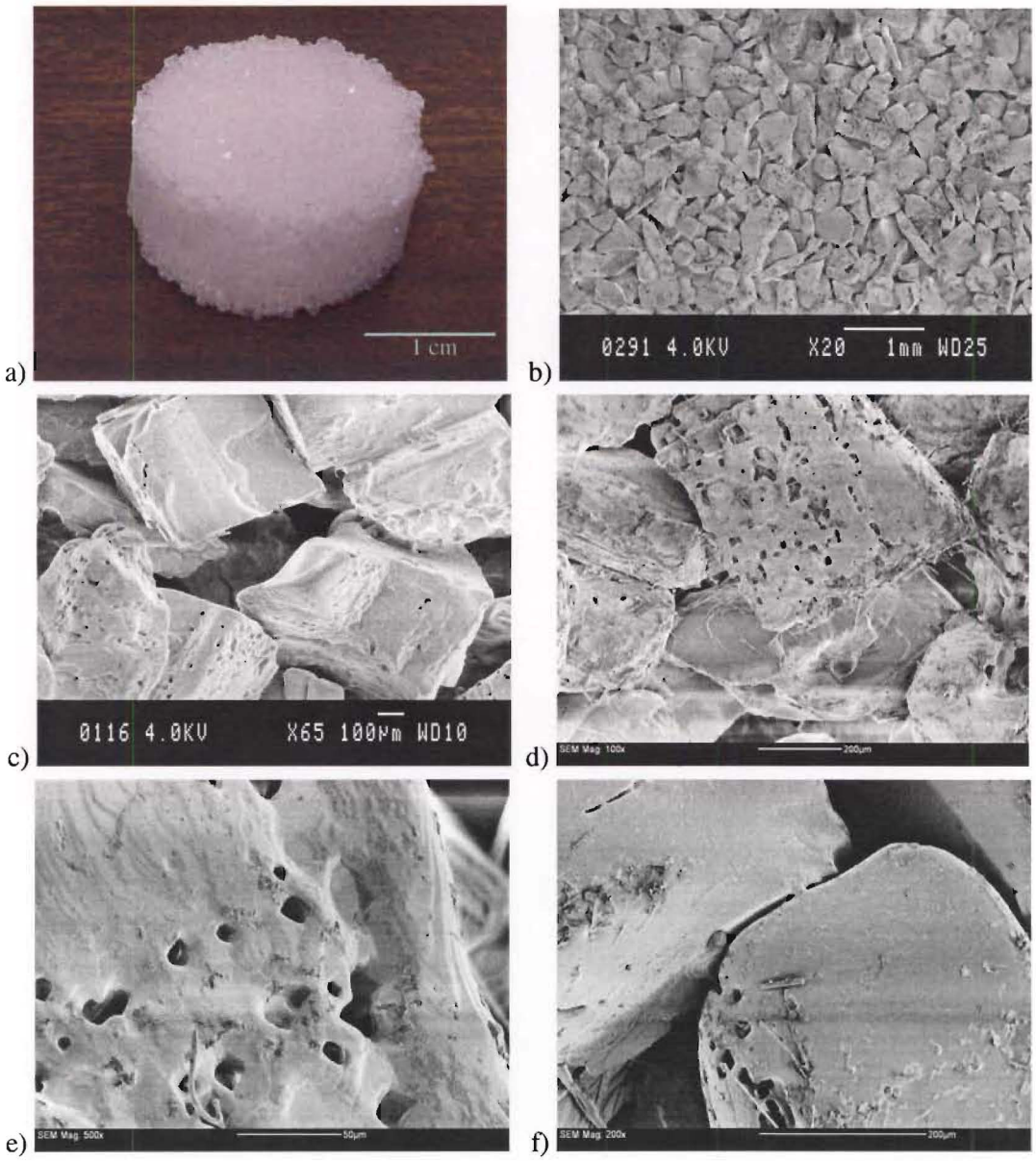

Figure 3.1 (a) A complete salt template strong enough to be handled and (b-f) SEM micrographs showing a salt template sintered at 800°C for 3 hours at various magnifications.

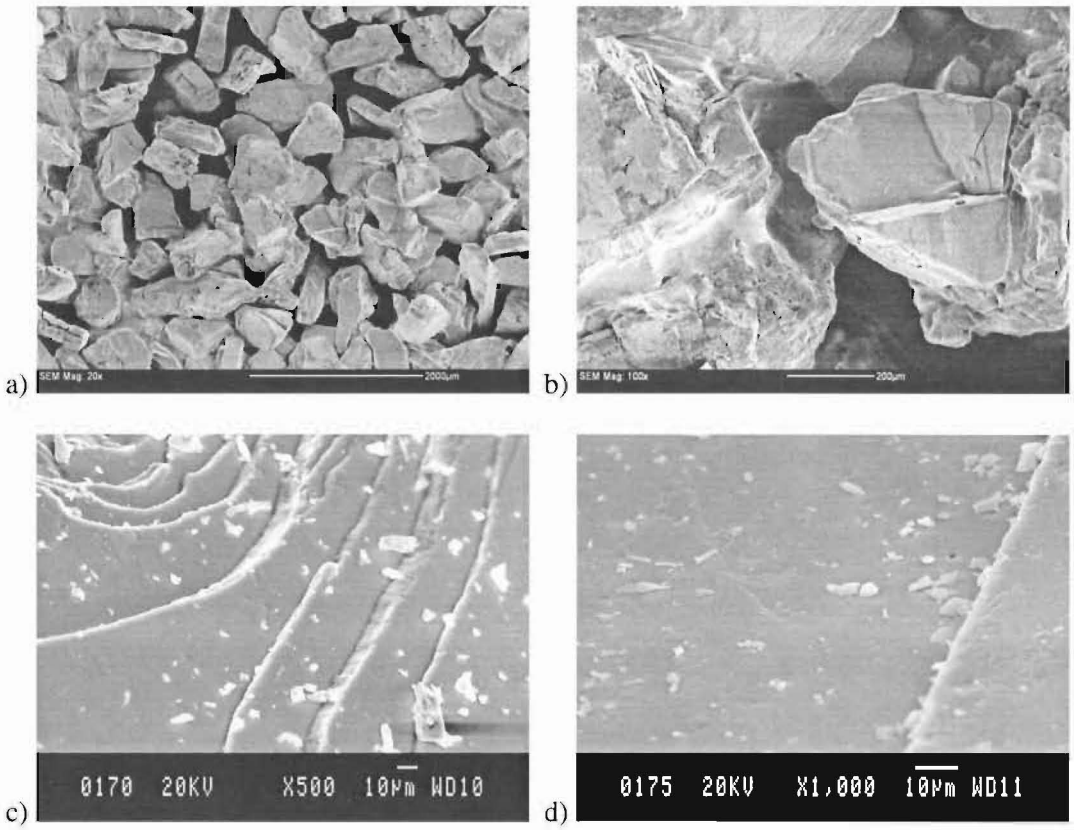

Figure 3.2 (a-d) SEM micrographs of raw salt particles prior to sintering at various magnifications.

A vertical cross section of a salt template (Figure 3.3 a) exhibits a network of interstice or pore throughout a template. This network provided a continuous path for liquid Mg during infiltration process. The pore sizes of the template were determined from 2D images obtained from µ-CT. The smallest pore diameters is the one of interest and, among the areas selected, was found to be ~75 µm which is approximately the size estimated previously (see 1.3.2.2) (Fig. 3.4b). This means that threshold pressure required for Mg infiltration should be 320 mbar, if θ is 150°, or less (see 1.3.2.2).

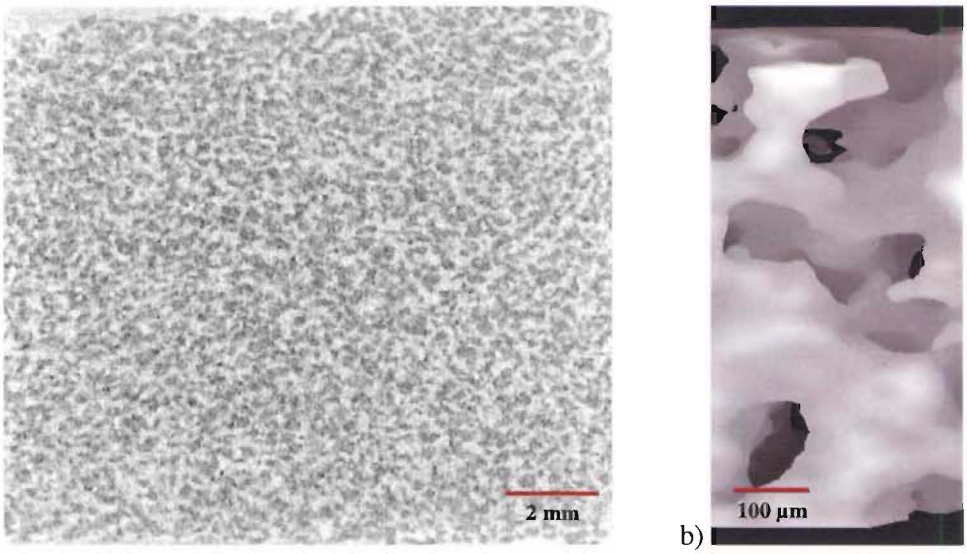

Figure 3.3 Structure of salt template a) Vertical-cut of salt template and b) 3D images obtained from Image J

Volume fractions of salt templates were determined by Image J and conventional method. Voxel counter plugin of Image J was operated and the values attained are listed in Table 3.1. The areas of interest were randomly selected throughout the whole structure of template with several sizes of determination. In conventional method, the mass and volume of salt template were first measured. Then the apparent density and finally volume fraction were attained.

Table 3.1 Volume fraction of sintered salt template

Random no.	By Image J (%)	Conventional method (%)
1	55.24	58.06
2	55.13	54.51
3	56.01	55.45
4	56.93	58.17
5	53.31	59.01
Ava.	**55.32**	**57.04**

It is worth noting that both techniques used to determine volume fraction of salt template have uncertainty drawn from their unavoidable limitations. The accuracy of results

obtained from Image J heavily relies on the level of threshold set and, unfortunately, the most appropriate threshold is always unknown. On the other hand, a few salt particles were observed to fall off the template during measuring. This inevitably alters mass and volume of the template and, hence, the resulting calculated salt volume fraction.

3.1.2 Mechanical Properties

It was found that the salt template obtained from sintering for 3 hrs was adequately strong for handling and casting. The compressive strength of the salt template is shown in Fig. 3.1. The ultimate compressive strength of angular salt template was ~316 kPa. There also seemed to some localised failure occurring shown by a small drop in load at a strain and stress of ~0.006 and ~78 kPa, respectively (point a). The elastic moduli of the template before and after this point were 13 and 15.21 MPa, respectively. These values suggest that the template should withstand the pressure during infiltration, which was previously predicted to be ~60 kPa.

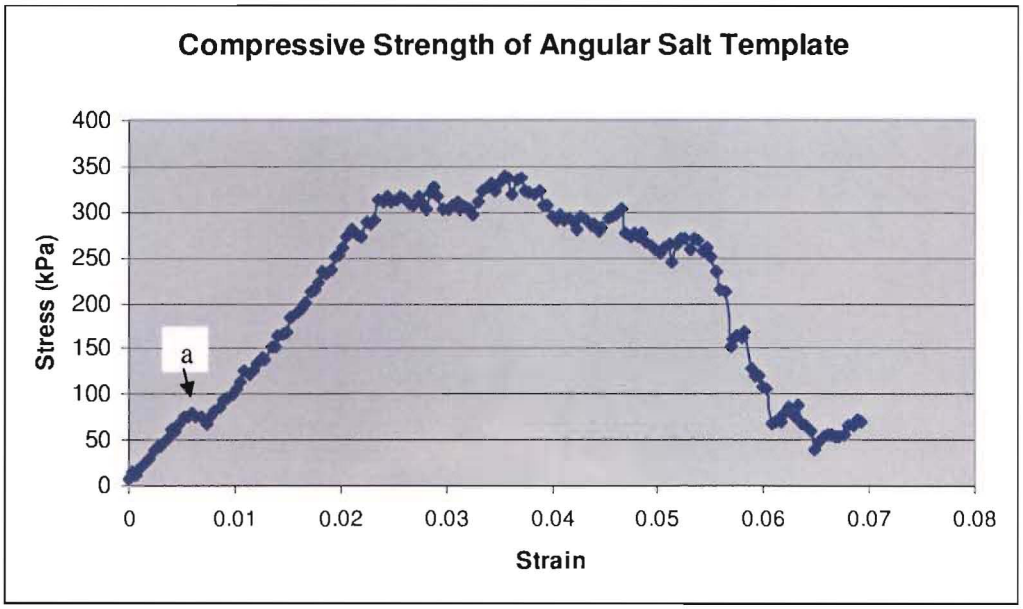

Figure 3.4 Compressive stress-strain curve of salt template

3.2 As-cast Mg-NaCl composite

The as-cast Mg-NaCl composite was cut and milled. The microstructure of the samples was observed by SEM (Fig. 3.5 (a-d)). In high magnification SEM no evidence of a reaction product could be observed to form at the Mg-NaCl interface. Liquid Mg completely infiltrated the salt template – however small gaps at the interface were observed as shown in Fig. 3.5d probably due to lack of wetting.

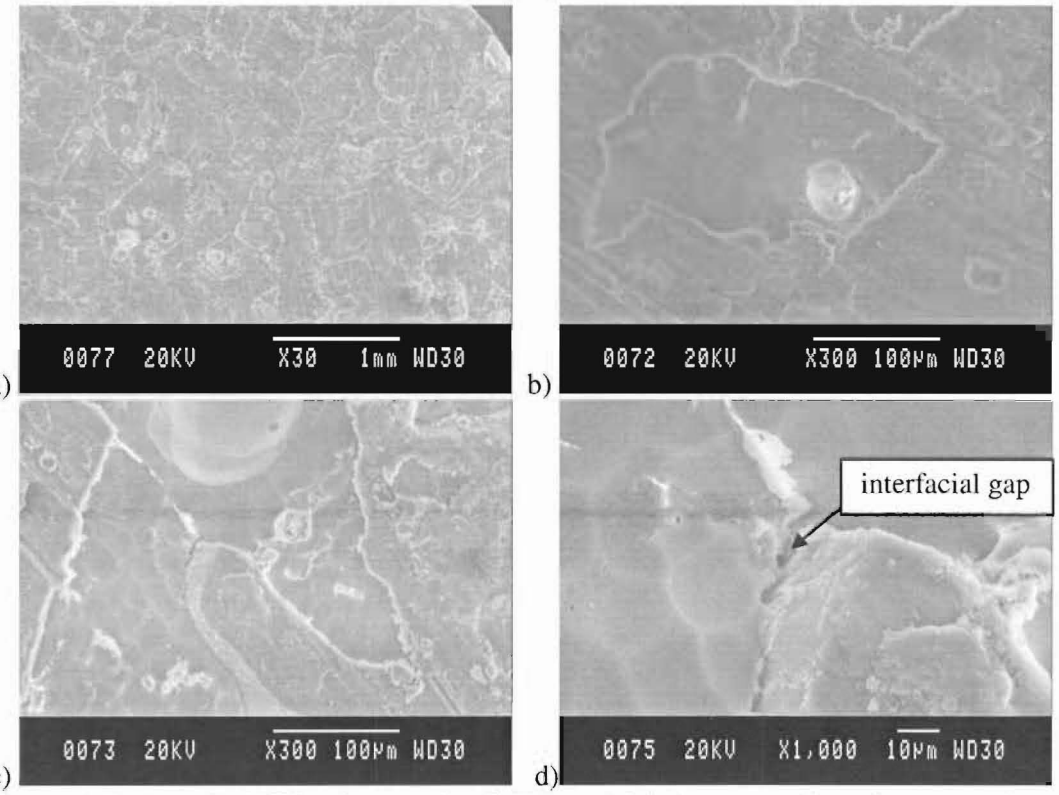

Figure 3.5 a) – d) SEM micrograph of as-cast Mg/salt composite taken at various magnifications.

The volume fraction of Mg and salt in the as-cast Mg-NaCl composite was determined using a law of mixtures approach. The densities of Mg and salt are 1.738 and 2.17 g/cm^3

respectively. Density of the composite samples, ρ_C, were then estimated using the following equation:

$$\rho_C = V_M \rho_M + (1 - V_M)\rho_F \quad 3.1$$

where V_M is the volume fraction of matrix material, ρ_M is density of matrix material and ρ_F is density of fibre or reinforcement material. The results are shown in Table 3.1.

Table 3.2 Volume fraction of Mg and salt in the composite calculated using The Law of Mixtures

Sample	*Mg vol. fraction (%)*	*Salt vol. fraction (%)*
1	0.669	0.331
2	0.661	0.339
3	0.664	0.336
4	0.653	0.347
5	0.700	0.300
6	0.673	0.327
Average	0.6700	0.3300

The volume fraction obtained tended to suggest unrealistically low volume fractions of salt and doubtfully high volume fractions of Mg. This situation suggests that voids may be present in as-cast Mg-NaCl composite due to incomplete infiltration. Using the measured density of the sintered salt template (see 3.1) and taking the volume of voids into account, the volume fraction of salt, Mg and voids were re-estimated to be around 55.3-57, 37-39 and 5.5-6% (Table 3.2). This method gives more rationale values of Mg volume fraction – however the actual value has to be obtained afterwards from real Mg foam. The high magnification SEM micrograph in Fig. 3.5 d revealed small gaps at the Mg-NaCl interface. However, the decisive conclusion cannot be drawn at the moment whether these interfacial gaps are responsible for the total void fraction of 5.5-6% and further work is required.

Table 3.3 Estimation of volume fraction of Mg and void based on previously measured volume fraction of salt template.

Assumption of salt volume fraction (%)	Average volume fraction of Mg (%)	Average volume fraction of void (%)
55.32	*39.12*	*5.555*
57.04	*36.98*	*5.98*

3.3 Microstructural characterisation of Mg foam

Mg-NaCl samples were immersed in a sodium hydroxide solution with a pH value >11.5 in order to leach the salt template from the Mg. SEM micrographs of the microstructure of the resulting Mg foam are shown in Fig. 3.6 (a)-(f). The pores in the resulting Mg foam have an angular shape, resembling the shape of the original salt particles. Therefore, there are thinner areas in the pore wall where deformation can initiate more easily when the foam is put under load (Fig.3.6c). Sharp edges will also act as crack initiation sites. These thin wall and sharp edge definitely reduce strength of Mg foam. The pores in Mg foam are observed to have both rough and smooth regions at the surface. This striking characteristic (see Fig. 3.6 e) appears to resemble the holes and surface topology of the sintered salt particle as shown in Fig 3.2 e).

a) 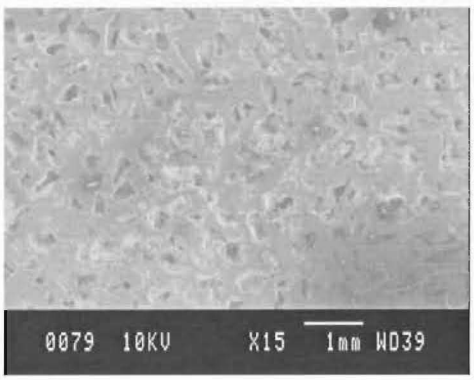

b) 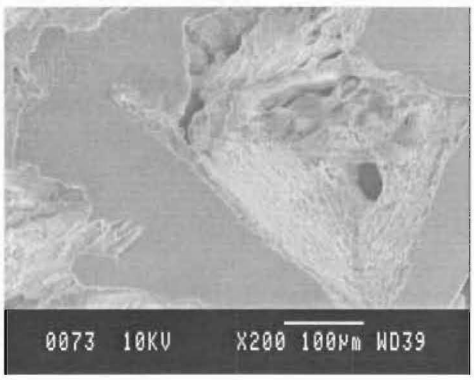

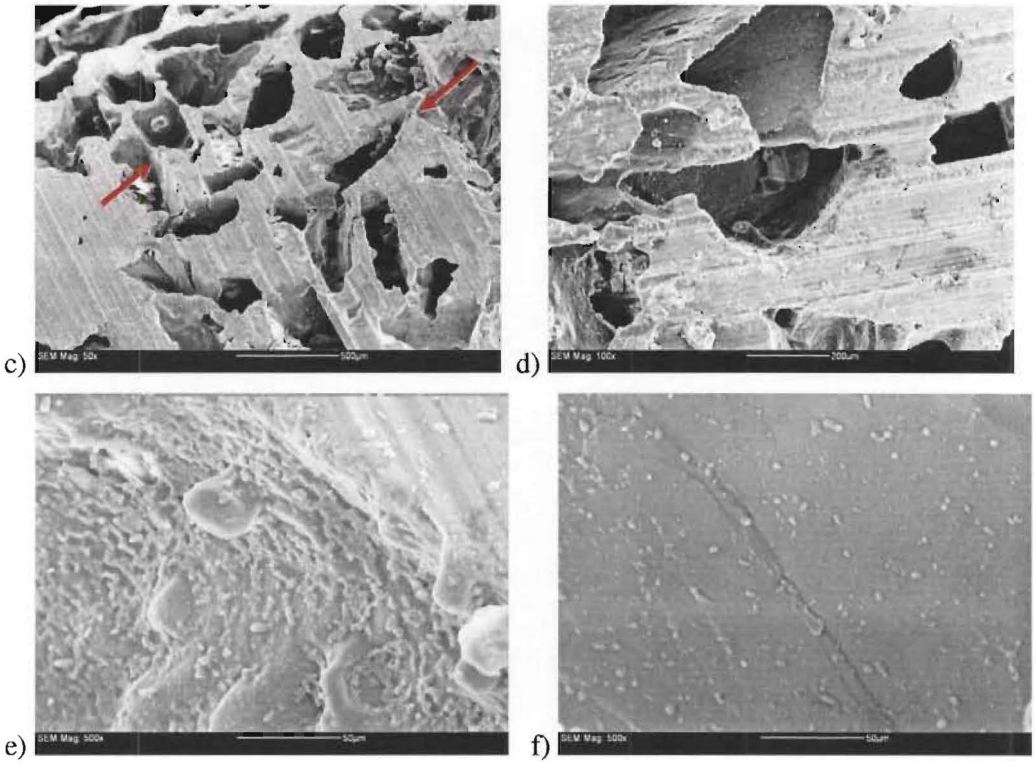

Figure 3.6 SEM micrographs of Mg foam at different magnifications. a)-d) The general structure of the foam, and e) rough and d) smooth internal pore surfaces in a Mg foam.

Structural 3D images of Mg foam were generated. An open-cell structure can be clearly seen as shown in Figure 3.7 a-j. The interconnectivity of pores in Mg foam is confirmed when 3D image of small area are generated as demonstrated in Figure 3.8 a-aj.

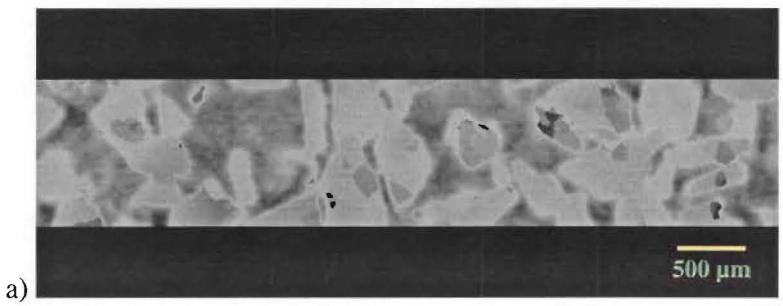

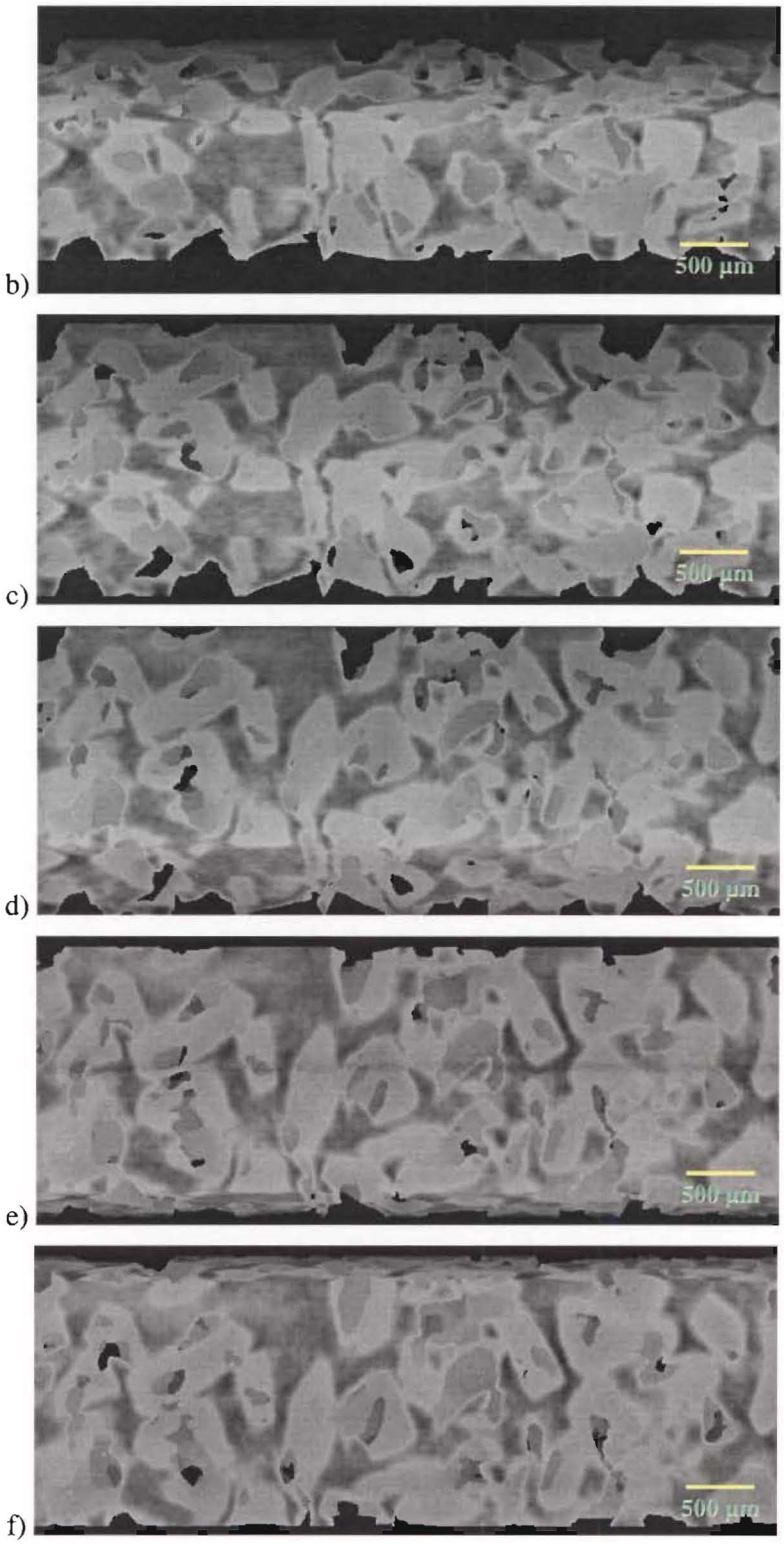
b)
500 µm
c)
500 µm
d)
500 µm
e)
500 µm
f)
500 µm

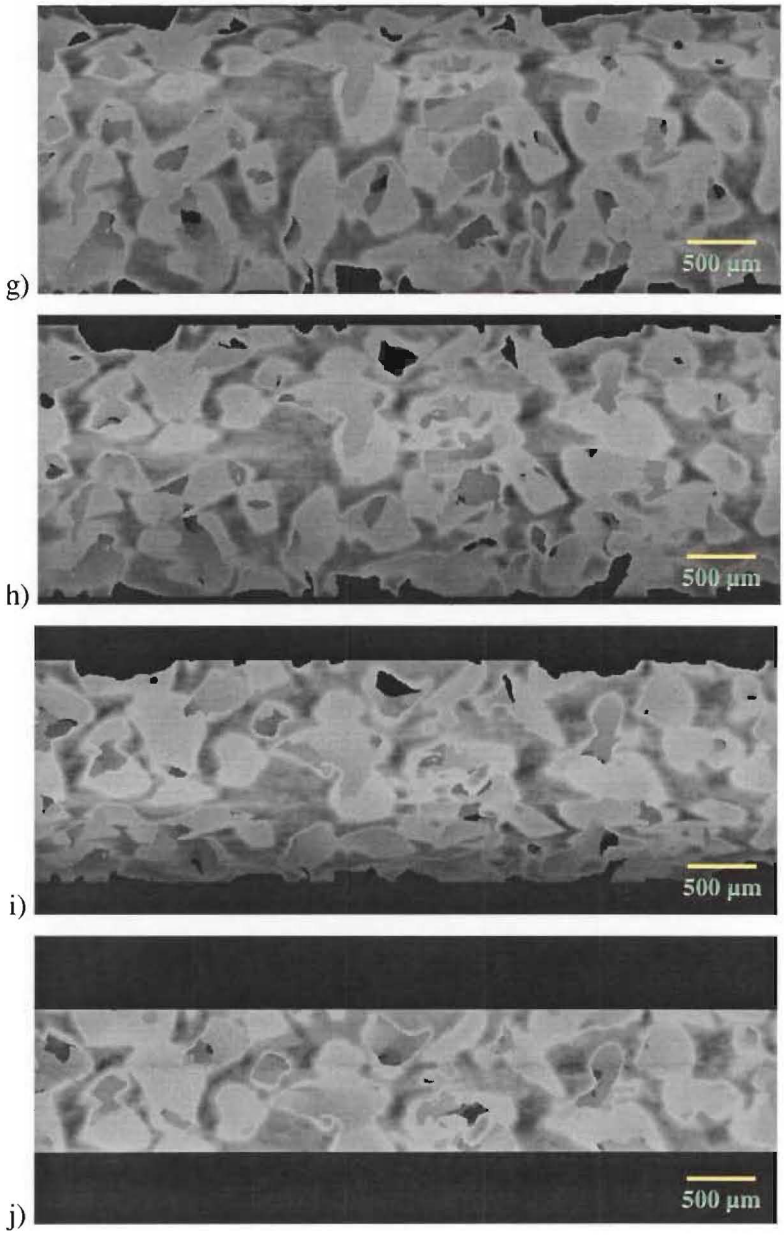

Figure 3.7 3D images of Mg foam with angular shape pore rotated on x axis with 20° increment. a) = 0°, b) = 20°, c) = 40°, d) = 60°, e) = 80°, f) = 100°, g) = 120°, h) = 140°, i) = 160° and j) = 180°.

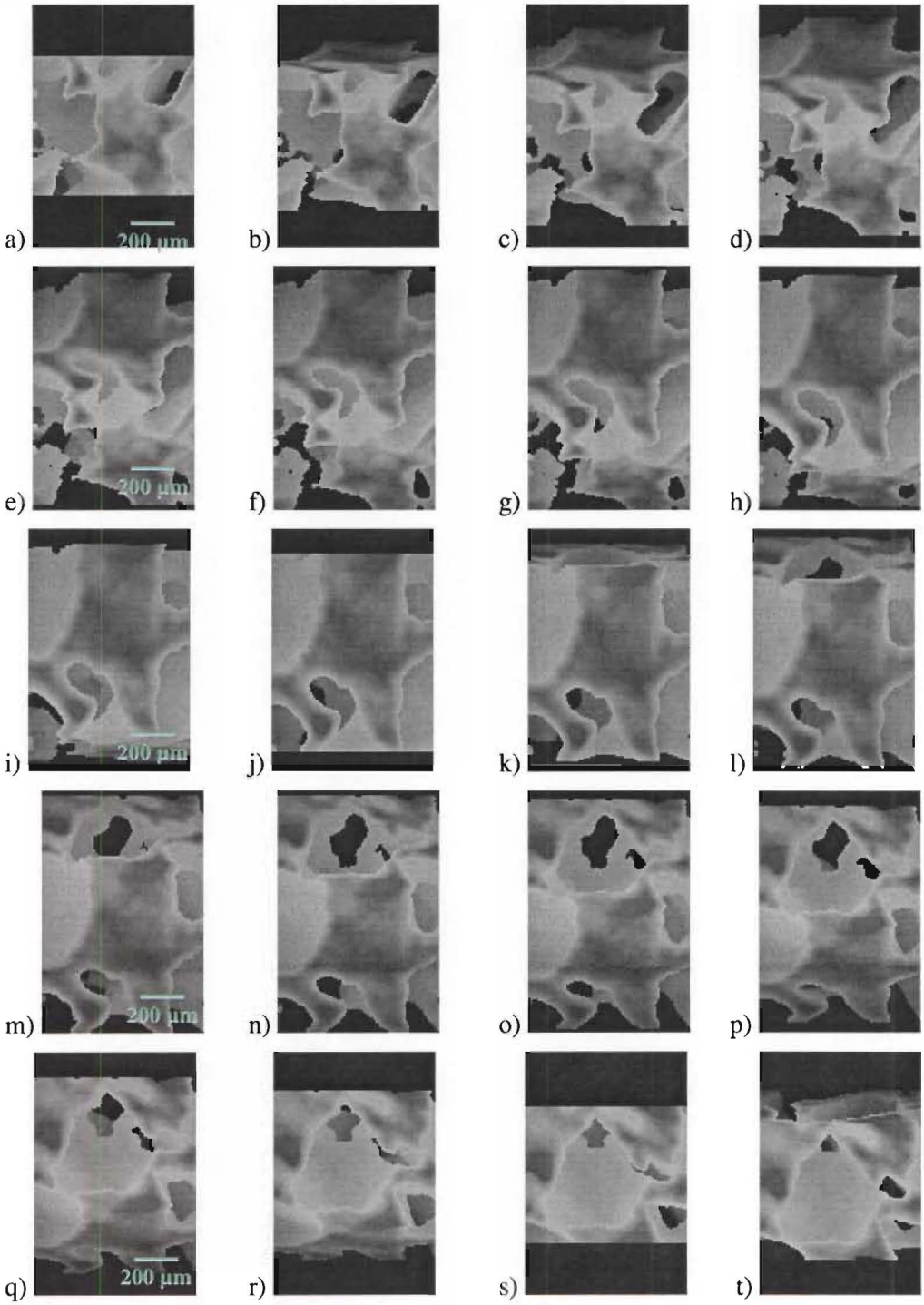
a)
200 µm
b)
c)
d)
e)
200 µm
f)
g)
h)
i)
200 µm
j)
k)
l)
m)
200 µm
n)
o)
p)
q)
200 µm
r)
s)
t)

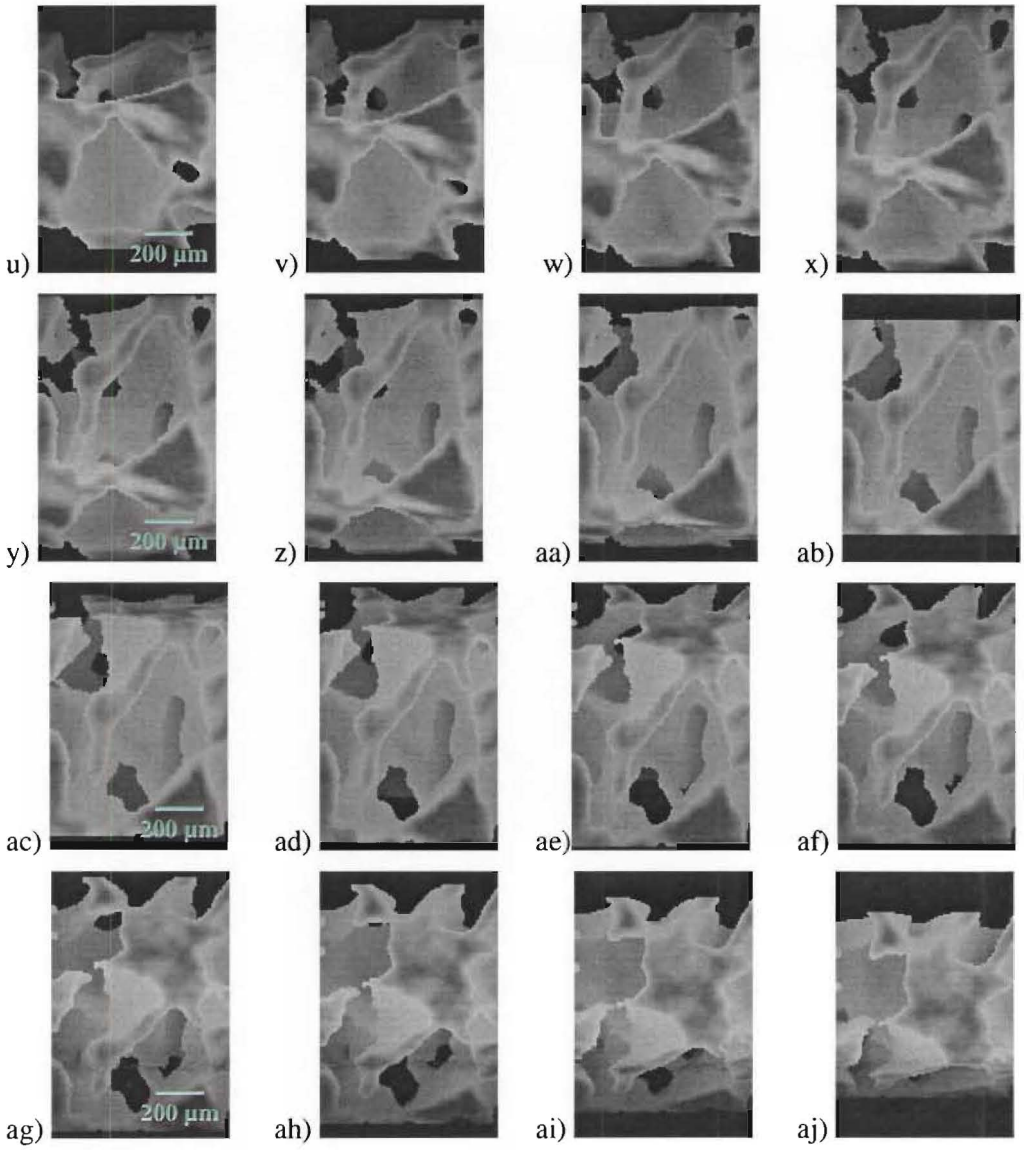

Figure 3.8 3D images of Mg foam with smaller area of interest rotated on x axis with 10° increment, i.e. a) = 0°, b) = 10°, c) = 30°,...ai) = 340° and aj) = 350°.

Range of pore size of Mg foam was gained from 2D images of µ-CT and was found to be in the same range of salt particle size (*i.e.* 422-599 µm). Pore interconnecting (or pore neck) size in Mg foam was also measured by 2D image analysis technique. Size of pore neck has an average of 134.76 µm with a minimum and maximum of 87 and 220.46 µm, respectively. This result, in over all, satisfies the recommended requirement of scaffold for bone tissue engineering that the interconnecting area of pore should be >100 µm. All

measured data, average and standard deviation (SD) of pore size and pore interconnecting size are provided in Table 3.4.

Table 3.4 Measured data of pore size and pore neck size of Mg foam

	Pore size	**Pore neck**
Measured values (μm)	465. 464.5, 566, 570, 431, 472.5, 476, 467.5, 592 and 433	157, 120.87, 220.46, 120, 143.28, 112, 140, 99.89, 109.41, 87, 138.07, 166.48, 104.2, 175.06, 127.65
Ava. (μm)	493.75	134.76
SD.	56.083	34.47

Volume fractions of Mg foam were also determined by Image J and conventional method. Voxel counter plugin of Image J was operated and the values attained are listed in Table 3.5. In conventional method, the mass and volume of salt template were first measured from a sample of 17 mm in diameter and 2.3 mm in thickness. Then the apparent density and finally volume fraction were attained. The values of volume fraction of Mg foam gained from both techniques showing that Mg foams may have porosity in range of 54.35-56.885%. These values of porosity are in agreement with the density of salt template previously reported in Section 3.1; however, it is somewhat different from the Mg volume fraction estimated in Table 3.2.

Table 3.5 Volume fraction of Mg foam

Random no.	By Image J (%)	Conventional method (%)
1	47.86	43.115
2	48.54	-
3	45.22	-
4	45.56	-
5	41.07	-
Ava.	**45.65**	**43.115**

3.4 Compressive properties of Mg foam

The compressive stress-strain curves of the Mg foam samples obtained in this work displayed a limited region of linear elasticity and an extended region involving plastic deformation and collapse of foam cell walls or struts (Fig 3.7). The densification region that is typically observed for metal foams is not shown in Fig 3.7 as the compressive tests were stopped before this point was reached. A summary of the mechanical properties of 3 samples is provided in Table 3.1.

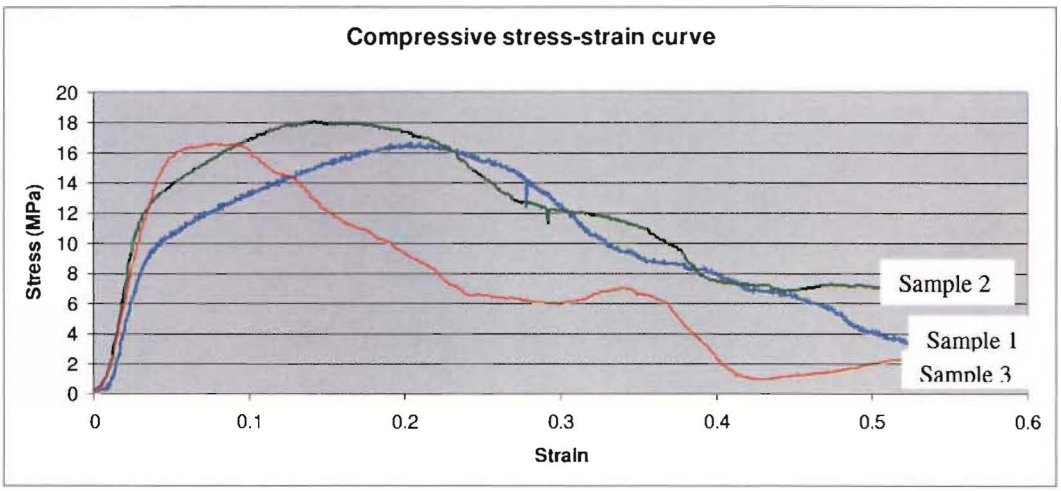

Figure 3.9 Compressive stress-strain behaviour of Mg foam.

Table 3.6 Mechanical properties of Mg foam

Sample	**#1**	**#2**	**#3**	*Average*
0.2% compressive yield strength (MPa)	8	11.1	14.3	*11.13*
Ultimate compressive strength (MPa)	16.4	17.8	16.5	*16.9*
Elastic modulus (GPa)	0.42	0.56	0.46	*0.48*

There was considerable variation in the stress-strain curve amongst the samples tested. This might due to non-uniformities in the cell wall thickness due to using angular salt particles to produce the template. The results showed that the actual elastic modulus of

Mg foam obtained in this work is at the low end of predicted values (see 1.2.3), while the compressive strength is within the predicted range, as shown in Fig. 3.8.

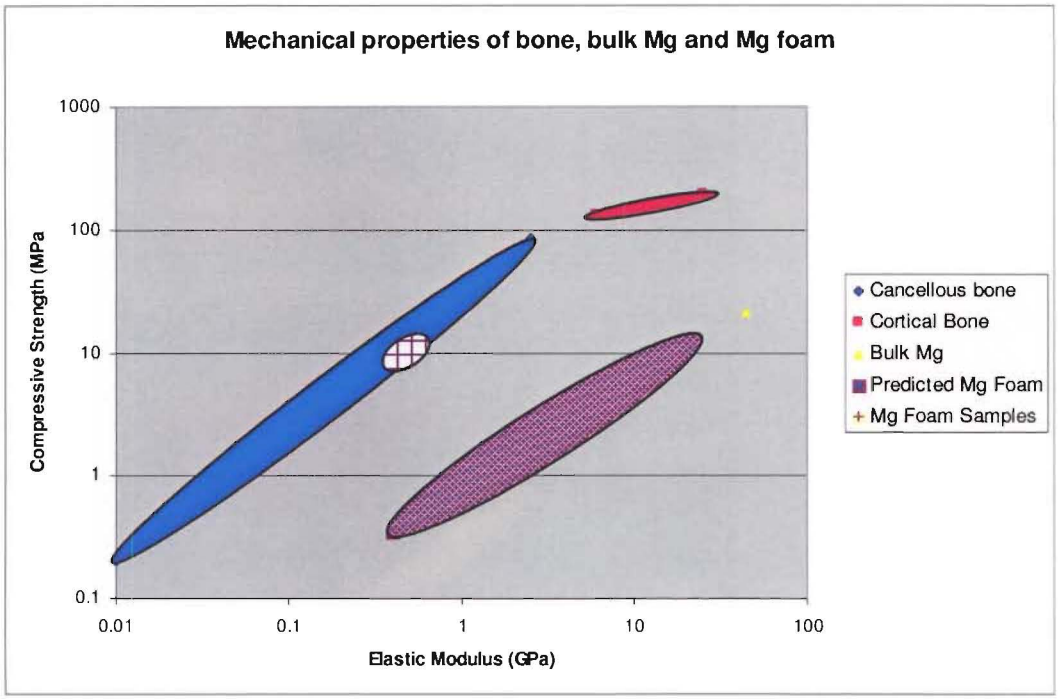

Figure 3.10 Comparison between actual mechanical properties of Mg foam and predicted values

4. Conclusions

This work has demonstrated that:

- An interconnected porous salt template could be used in conjunction with a liquid metal infiltration process to fabricate a Mg foam.
- Mg and salt do not appear to react during the infiltration process although further work will be required to confirm this using Differential Thermal Analysis (DTA).
- Mg foam with an open-cell, interconnected porous structure of about ~55% porosity can be obtained by immersing the Mg-NaCl composite into a water-based solution with a pH >11.5 to leach out the salt.
- The final pore size and shape of Mg foam was found to closely replicate that of the sintered salt particles. Therefore precise control over resulting Mg foam is highly possible.
- The compressive properties of the produced Mg foam were found to be more akin to human cancellous bone compared with conventional metallic biomaterials. However, Mg foam has an elastic modulus far lower than the estimated value using empirical models suggesting the process can be further optimised.

5. Future work

It is broadly accepted that mechanical properties of metal foams depends greatly on inherit properties of material which it is made, foam density and its structure [82]. Therefore, further work to improve mechanical properties of Mg foam can be an improvement through an alteration in either relative density of the structure or the way the structure is constructed. According to the models for estimation of mechanical properties of cellular materials present in Table 1.4, the relative density can vary the elastic modulus and compressive strength of metal foam to the power 2 and 3/2, respectively. On the other hand, the structure of metal foam influences the elastic modulus and compressive strength by altering the model constant used in the models. Using models in Table 4 and mechanical testing data from this work to calculate back to obtain the constant it was found that:

- The model constant for modulus from this work was only 0.046-0.068 while what recommended is in the range of 0.1-4.
- The model constant for compressive yield strength from this work was >1.23.

It is attention-grabbing to find out the cause of a large gap occur in case of modulus.

The use of spherical salt particles for producing the NaCl template is recommended in future work. Fig. 5.1 illustrates the structure of salt templates obtained from both angular and spherical salt particles. Particle connecting patterns of angular particles can be edge-to-edge, face-to-edge or face-to-face while there is only point-to-point connecting type for spherical particle. Thus, spherical salt particles should result in a more uniform pore

structure and improvements in the ultimate compressive strength. It is also interesting to study whether using spherical salt particle can significantly change the structure of the foam and, subsequently plus hopefully, can improve the modulus.

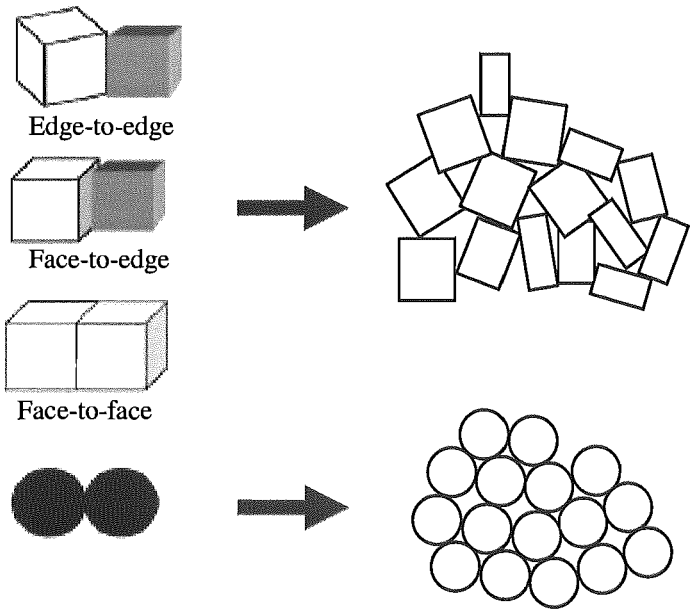

Figure 5.1 Diagrams of structure of template obtained from angular and spherical particles

Another benefit from using spherical salt particle might be the reduction time in sintering process [41]. On way to produce spherical particle of salt is to quickly pass angular salt particles through the heat source to superficially melt the particle. The fast transformation from liquid to solid causes the contraction resulting in the formation of voids and the development of residual stress on the surface of particles. This stress behaves as a preserved energy that can shorten the sintering process [41].

References

1. Jones, J.R. & Hench, L.L., *Biomedical materials for new millennium: Perspective on the future.* Materials Science and Technology, 2001. **17**(8): p. 891-900.
2. Niinomi, M., *Recent metallic materials for biomedical applications.* Metallurgical and Materials Transactions, 2002. **33A**: p. 477-486.
3. Park, J.B. & Kim, Y.K., *Metallic biomaterials*, in *Biomaterials: Principles and applications*, J.B. Park and J.D. Bronzino, Editors. 2003, CRC Press LLC,: United States of America. p. 1-20.
4. Dee, K.C., Puleo, D.A., & Bizios, R., *Tissue-biomaterials interactions.* 2002, United States of America: John Wiley & Sons, Inc.
5. Jacobs, J.J., et al., *Metal degradation products: A cause for concern in metal-metal bearing?* Clinical Orthopaedics and Related Research, 2003. **417**: p. 139-147.
6. Lhotka, C., et al., *Four-year study of cobalt and chromium blood levels in patients managed with two different metal-on-metal total hip replacements.* Journal of Orthopaedic Research, 2003. **21**: p. 189-195.
7. Jacobs, J.J., Gilbert, J.L., & Urban, R.M., *Corrosion of metal orthopaedic implants.* Journal of Bone and Joint Surgery, 1998. **80-A**(2): p. 268-282.
8. Jacobs, J.J., et al., *Metal release in patients who have had a primary total hip arthroplasty: A prospective controlled, longitudinal study.* Journal of Bone and Joint Surgery, 1998. **80-A**: p. 1447-1458.
9. Puleo, D.A. & Huh, W.W., *Acute toxicity of metal Ions in cultures of osteogenic cells derived from bone marrow stromal cells.* Journal of Applied Biomaterials, 1995. **6**: p. 109-116.
10. Buchman, A., *The next generation in medical implants.* Materials World, 2004. **12**(2): p. 26-28.
11. Nagels, J., Stokdijk, M., & Rozing, P.M., *Stress shielding and bone resorption in shoulder arthroplasty.* Journal of Shoulder and Elbow Surgery, 2003. **12**(1): p. 35-39.
12. Bonfield, W., *Biomaterials: Research and development.* Materials: Science and application, Access(1 June 2003): http://www.mpg.de/pdf/europeanWhiteBook/wb_materials_068_113.pdf.
13. Troitskii, V.V. & Tsitrin, D.N., *The resorbing metallic alloy 'Osteosinthezit' as material for fastening broken bone.* Khirurgiia, 1944. **8**: p. 41-44.
14. Znamenskii, M.S., *Metallic osteosynthesis by means of an apparatus made of resorbing metal.* Khirurgiia, 1945. **12**: p. 60-63.
15. Hutmacher, D.W., *Scaffolds in tissue engineering bone and cartilage.* Biomaterials, 2000. **21**(24): p. 2529-2543.
16. *Biomaterials availability: Potential effects on medical innovation and health care.* 2000 Access(13 Apr 2004): http://www.rand.org/publications/IP/IP194/IP194.pdf.
17. Access(23/10/2005): http://www.medterms.com/script/main/art.asp?articlekey=22068.
18. Currey, J.D., *Bones: Structure and mechanics.* 2002, New Jersey, USA: Princeton University Press. 3-26.

19. Guyton, A.C. & Hall, J.E., *Parathyroid hormone, calcitonin, calcium and phosphate metabolism, vitamin D, bone, and teeth*, in *Textbook of medical physiology*. 2000, W. B. Saunders Company: Philadelphia, USA.
20. Lees, R.L., Sabharwal, V.K., & Heersche, J.N.M., *Resorptive state and cell size influence intracellular pH regulation in rabbit osteoclasts cultured on collagen-hydroxyapatite films*. Bone, 2001. **28**(2): p. 187-194.
21. Madyastha, P.R., et al., *IFN-g enhances osteoclast generation in cultures of peripheral blood from osteopetrotic patients and normalizes superoxide production*. Journal of Inte20feron & Cytokine Research, 2000. 7(645-652).
22. Bonfield, W., *Artificial bone*, in *Concise encyclopedia of composite materials*, A. Kelly, Editor. 1994, Elsevier Science Ltd.: Great Britain. p. 15-17.
23. Gibson, L.J. & Ashby, M.F., *Cancellous bone*, in *Cellular solids: Structure and properties*. 1997, Cambridge University Press: Great Britain. p. 429-452.
24. Pritchard, J.J., *General history of bone*, in *The biochemistry and physiology of bone*, G.H. Bourne, Editor. 1972, Academic Press: New York and London.
25. Vaughan, J.M., *The physiology of bone*. 1970, Oxford: Clarendon Press.
26. Daculsi, G., Bouler, J.-M., & LeGeros, R.Z., *Adaptive crystal formation in normal and pathological calcifications in synthetic calcium phosphate and related biomaterials*, in *International review of cytology*, K.W. Jeon, Editor. 1997, Academic Press: United States of America. p. 129-191.
27. Dorozhkin, S.V. & Epple, M., *Biological and medical significance of calcium phosphates*. Angewandte Chemie International Edition, 2002. **41**(17): p. 3130-3146.
28. Lee, H.B., Khang, G., & Lee, J.H., *Polymeric biomaterials*, in *Biomaterials: Principles and applications*, J.B. Park and J.D. Bronzino, Editors. 2003, CRC Press LLC: United States of America. p. 55-77.
29. Jallot, E., *Role of magnesium during spontaneous formation of a calcium phosphate layer at the periphery of a bioactive glass coating doped with MgO*. Applied Surface Science, 2003. **211**: p. 89-95.
30. Billotte, W.G., *Ceramics biomaterials*, in *Biomaterials: Principles and applications*, J.B. Park and J.D. Bronzino, Editors. 2003, CRC Press LLC: United States of America. p. 21-53.
31. Clarke, H. & Green, M., *Materials*, in *Engineering theory in orthopaedics: An introduction*, M. Green and L.D.M. Nokes, Editors. 1988, Ellis Horwood Ltd.: Great Britain. p. 13-47.
32. Smith, G.K., *Orthopaedic biomaterials*. Access(8 Sep. 2004): http://www.ivis.org/special_books/ortho/chapter_13/13mast.asp.
33. Haynes, D.R., et al., *Variation in cytokines induced by particles from different prosthetic materials*. Clinical Orthopaedics and Related Research, 1998. **352**: p. 223-230.
34. Bi, Y., et al., *Titanium particles stimulate bone resorption by inducing differentiation of murine osteoclasts*. Journal of Bone and Joint Surgery, 2001. **83-A**: p. 501-508.
35. Allen, M.J., et al., *The effects of particulate cobalt, chromium and cobalt-chromium alloy on human osteoblast-like cells in vitro*. Journal of Bone and Joint Surgery, 1997. **79-B**: p. 475-482.
36. Wang, M.L., et al., *Titanium particles suppress expression of osteoblastic phenotype in human mesenchymal stem cells*. Journal of Orthopaedic Research, 2002. **20**: p. 1175-1184.

37. Niki, Y., et al., *Metal ions induce bone-resorbing cytokine production through the redox pathway in synoviocytes and bone marrow macrophages.* Biomaterials, 2003. **24**: p. 1447-1457.
38. Granchi, D., et al., *Cytokine release in mononuclear cells of patients with Co-Cr hip prosthesis.* Biomaterials, 1999. **20**: p. 1079-1086.
39. Wang, J.Y., et al., *Titanium, chromium and cobalt ions modulate the release of bone-associated cytokines by human monocytes/macrophages in vitro.* Biomaterials, 1996. **17**: p. 2233-2240.
40. Burg, K.J.L., Porter, S., & Kellam, J.F., *Biomaterial developments for bone tissue engineering.* Biomaterials, 2000. **21**(23): p. 2347-2359.
41. Gross, K.A. & Rodriguez-Lorenzo, L.M.L.M., *Biodegradable composite scaffolds with an interconnected spherical network for bone tissue engineering.* Biomaterials, 2004. **25**(20): p. 4955-4962.
42. Atwood, R.C., et al., *Analysis of pore interconnectivity in bioactive glass foams using X-ray microtomography.* Scripta Materialia, 2004. **51**(11): p. 1029-1033.
43. Burg, K.J.L., Porter, S., & Kellam, J.F., *Biomaterial developments for bone tissue engineering.* Biomaterials, 2000. **21**: p. 2347-2359.
44. Borden, M., et al., *Tissue engineered microsphere-based matrices for bone repair: design and evaluation.* Biomaterials, 2002. **23**: p. 551-559.
45. Jones, J.R., Ehrenfried, L.M., & Hench, L.L., *Optimising bioactive glass scaffolds for bone tissue engineering.* Biomaterials. **article in press**.
46. Karageorgiou, V. & Kaplan, D., *Porosity of 3D biomaterial scaffolds and osteogenesis.* Biomaterials, 2005. **26**(27): p. 5474-5491.
47. Flautre, B., et al., *Porous HA ceramics for bone replacement: Role of the pores and interconnections - experimental study in the rabbit.* Journal of Materials Science: Materials in Medicine, 2001. **12**: p. 679-682.
48. Pilliar, R.M., *P/M processing of surgical implants: Sintered porous surfaces for tissue-to-implant fixation.* The International Journal of Powder Metallurgy, 1998. **34**(8): p. 33-45.
49. Frosch, K.-H., et al., *Migration, matrix production and lamellar bone formation of human osteoblast-like cells in porous titanium implants.* Cells Tissues Organs, 2002. **170**(4): p. 214-227.
50. Chang, B.-S., et al., *Osteoconduction at porous hydroxyapatite with various pore configurations.* Biomaterials, 2000. **21**(12): p. 1291-1298.
51. Yuan, H., et al., *A preliminary study on osteoinduction of two kinds of calcium phosphate ceramics.* Biomaterials, 1999. **20**(19): p. 1799-1806.
52. Yang, Z.J., et al., *Osteogenic responses to extraskeletally implanted synthetic porous calcium phosphate ceramics: an early stage histomorphological study in dogs.* Journal of Materials Science: Materials in Medicine, 1997. **8**: p. 697-701.
53. Daculsi, G., LeGeros, R.Z., & Heughebaert, M., *Formation of carbonate apatite crystals after implantation of calcium phosphate ceramics.* Calcified Tissue International, 1990. **46**: p. 20-27.
54. Kawai, N., et al., *Bone formation by cells from femurs cultured among three-dimensionally arranged hydroxyapatite granules.* Journal of Biomedical Materials Research, 1997. **37**: p. 1-8.
55. D'Lima, D.D., et al., *Bone response to implant surface morphology.* Journal of Arthroplasty, 1998. **13**(8): p. 928-934.

56. Lampin, M., et al., *Correlation between substratum roughness and wettability, celladhesion, and cell migration.* Journal of Biomedical Materials Research, 1997. **36**(1): p. 99-108.
57. Sul, Y.-T., et al., *Qualitative and quantitative observations of bone tissue reactions to anodised implants.* Biomaterials, 2002. **23**: p. 1809-1817.
58. Okuma, T., *Magnesium and bone strength.* Nutrition, 2001. **17**: p. 679-680.
59. Wolf, F.I. & Cittadini, A., *Chemistry and biochemistry of magnesium.* Molecular Aspects of Medicine, 2003. **24**: p. 3-9.
60. Guyton, A.C. & Hall, J.E., *Integration of renal mechanisms*, in *Textbook of medical physiology.* 2000, W. B. Saunders Company: Philadelphia, USA.
61. Vormann, J., *Magnesium: nutrition and metabolism.* Molecular Aspects of Medicine, 2003. **24**: p. 27-37.
62. Saris, N.-E.L., et al., *Magnesium: An update on physiological, clinical and analytical aspects.* Clinica Chimica Acta, 2000. **294**: p. 1-26.
63. Hartwig, A., *Role of magnesium in genomic stability.* Mutation Research/Fundamental and Molecular Mechanisms of Mutagenesis, 2001. **475**: p. 113-121.
64. Maly, E., *Carcinogenesis from the standpoint of view of molecular geometry and synergism: Relevance of oxygen and magnesium.* Medical Hypotheses, 1983. **11**: p. 177-184.
65. Scholz, W., *Support or holding unit for insertion into a bone, consists of a material which breaks down, eg magnesium, and contains hollow areas that hold medicaments.* 2004, Patent: DE10241572: Germany.
66. Blumenthal, B. & Hadenfeldt, H., *Materials for surgical ligatures and sutures.* 1937, Patent: 2094578: US.
67. Kuwahara, H., et al., *Precipitation of magnesium apatite on pure magnesium surface during immersing in Hank's solution.* Materials Transactions, 2001. **42**: p. 1317-1321.
68. Stroganov, G.B., et al., *Magnesium-base alloys for use in bone surgery.* 1972, Patent: 3687135: US.
69. Seelig, M.G., *A study of magnesium wire as an absorbable sature and ligature materila.* Archives of Surgery, 1924. **8**: p. 669-680.
70. Witte, F., et al., *Characterization of degradable magnesium alloys as orthopeadic implant material by synchrotron-radiation-based microtomography.* Access(8 Sep. 2004): http://www-hasylab.desy.de/science/annual_reports/2001_report/part1/contrib/47/5461.pdf.
71. Kaesel, V., et al., *Approach to control the corrosion of magnesium alloys and their applications*, in *Proceedings of the 6th international conference magnesium alloys and their applications*, K.U. Kainer, Editor. 2004, Wiley-Vch. p. 534-539.
72. Takaya, M., Hashimoto, K., & Toda, Y., *Application of magnesium to biomaterials for hard-tissue.* Journal of Japan Institute of Light Metals, 2000. **50**(7): p. 343-347.
73. Li, L., Gao, J., & Wang, Y., *Evaluation of cyto-toxicity and corrosion behavior of alkali-heat-treated magnesium in simulated body fluid.* Surface and Coatings Technology, 2004. **185**: p. 92-98.
74. Anastassopoulou, J. & Theophanides, T., *Magnesium-DNA interactions and the possible relation of magnesium to carcinogenesis. Irradiation and free radicals.* Critical Reviews in Oncology/Hematology, 2002. **42**: p. 79-91.

75. Stevens, A.J. & Wolff, H.G., *Magnesium intoxication: Absorption form the intact gastrointestinal tract.* Archives of Neurology: p. 749-759.
76. Yamasaki, Y., et al., *Synthesis of functionally graded MgCo3 apatite accerelating osteoblast adhesion.* Journal of Biomedical Materials Research, 2002. **62**: p. 99-105.
77. Yamasaki, Y., et al., *Action of FGMgCO3Ap-collagen composite in promoting bone formation.* Biomaterials, 2003. **24**: p. 4913-4920.
78. Siebers, M.C., et al., *Integrins as linker proteins between osteoblasts and bone replacing materials. A critical review.* Biomaterials, 2005. **26**: p. 137-146.
79. Webster, T.J., et al., *Osteoblast response to hydroxyapatite doped with divalent and trivalent cations.* Biomaterials, 2004. **25**: p. 2111-2121.
80. Revell, P.A., et al., *The effect of magnesium ions on bone bonding to hydroxyapatite.* Key Engineering Materials, 2004. **254-256**: p. 447-450.
81. Serre, C.M., et al., *Influence of magnesium substitution on a collagen-apatite biomaterial on the production of a calcifying matrix by human osteoblasts.* Journal of Biomedical Materials Research, 1998. **42**(4): p. 626-633.
82. Ashby, M.F., et al., *Metal foams: A design guide.* 2000, United States of America: Butterworth-Heinemann.
83. Clyne, T.W. & Withers, P.J., *Fabrication processes*, in *An introduction to metal matrix composites.* 1993, Cambridge University Press: Cambridge. p. 318-369.
84. Banhart, J., *Manufacture, characterisation and application of cellular metals and metal foams.* Progress in Materials Science, 2001. **46**(6): p. 559-632.
85. Korner, C., et al., *Endogenous particle stabilization during magnesium integral foam production.* Advanced Engineering Materials, 2004. **6**(6): p. 385-390.
86. Wen, C.E., et al., *Processing of biocompatible porous Ti and mg.* Scripta Materialia, 2001. **45**(10): p. 1147-1153.
87. Wen, C.E., et al., *Porous biodegradable magnesium as bone substitute.* Materials Science Forum, 2003. **419-422**: p. 1001-1006.
88. Yamada, Y., et al., *Processing of an open-cellular AZ91 magnesium alloy with a low density of 0.05 g/cm^3.* Journal of Materials Science Letters, 1999. **18**: p. 1477-1480.
89. Hartmann, M., Reindel, K., & Singer, R.F., *Fabrication and properties of syntactic magnesium foams.* Mat. Res. Soc. Symp. Proc., 1998. **521**: p. 211-216.
90. Jiang, B., et al., *A novel method for making open cell aluminium foams by powder sintering process.* Materials Letters, 2005. **59**: p. 3333-3336.
91. Wen, C.E., et al., *Compressibility of porous magneium foam: dependency on porosity and pore size.* Materials Letters, 2004. **58**: p. 357-360.
92. Chaing, Y.-M., Brinie, D.P., & Kingery, W.D., *Physical ceramics: Principles for ceramic science and engineering.* 1997, United States of America: John Wiley & Sons.
93. Hull, D. & Clyne, T.W., *An introduction to composite materials.* Cambridge solid state science, ed. D.R. Clarke, S. Suresh, and I.M. Ward FRS. 1996, Cambridge: Cambridge University Press.
94. Muscat, D., Harris, R.L., & Drew, R.A.L., *The effect of pore size on the infiltration kinetics of aluminum in titanium carbide preforms.* Acta Metallurgica et Materialia, 1994. **42**(12): p. 4155-4163.
95. Garcia-Cordovilla, C., Louis, E., & Narciso, J., *Pressure infiltration of packed ceramic particulates by liquid metals.* Acta Materialia, 1999. **47**: p. 4461-4479.

96. Mortensen, A. & Cornie, J., *On the infiltration of metal matrix composite.* Metallurgical Transactions A, 1987. **18A**: p. 1160-1163.
97. Martins, G.P., Olson, D.L., & Edwards, G.R., *Modeling of infiltration kinetics for liquid metal processing of composites.* Metallurgical Transactions, 1988. **19B**: p. 95-101.
98. Molina, J.M., et al., *Threshold pressure for infiltration and particle specific surface area of particle compacts with bimodal size distributions.* Scripta Materialia, 2004. **51**(6): p. 623-627.
99. Aghajanian, M.K., et al., *The fabrication of metal matrix composites by a pressureless infiltration technique.* Journal of Materials Science, 1991. **26**: p. 447-454.
100. German, R.M., *Sintering theory and practice.* 1996, United States of America: John Wiley & Sons, Inc. 147-149.
101. Ammar, A.A. & Budworth, D.W., *Sintering of sodium chloride.* The Proceedings of British Ceramic Society, 1965. **3**: p. 185-193.
102. San Marchi, C. & Mortensen, A., *Infiltration and the replication process for producing metal sponges*, in *Handbook of cellular metals: Production, processing, applications*, H.-P. Degischer and B. Kriszt, Editors. 2002, Wiley-VCH Verlag GmbH: Federal Replublic of Germany. p. 43-56.
103. Cochran, C.N., *Production of reinforced composites.* 1970, Patent: US3547180: United States of America.
104. Cook, A.J., *Pressure infiltration casting of metal matrix composites.* Materials Science and Engineering, 1991. **A144**: p. 189-206.
105. Kainer, K.U. & Benzler, T.U., *Squeeze-casting and Thixo-casting of magnesium alloys*, in *Magnesium alloys and technology*, K.U. Kainer, Editor. 2003, Wiley-VCH Verlag GmbH &Co. KG aA: Federal Republic of Germany. p. 57.
106. Polonsky, L., Lipson, S., & Markus, H., *Lightweight cellular metal.* Modern Castings, 1961. **39**: p. 57-71.
107. Muylder, J.V. & Pourbaix, M.J.N., *Magnesium*, in *Atlas of electrochemical equilibria*, M.J.N. Pourbaix, Editor. 1966, Pergamon Press Ltd.: Great Britain. p. 139-145.
108. Witte, F., et al., *In vivo corrosion of four magnesium alloys and the associated bone response.* Biomaterials, 2005. **26**: p. 3557-3563.

Appendix 1: Human Skeleton